

## Article

# Acetylation of Eugenol on Functionalized Mesoporous Aluminosilicates Synthesized from Amazonian *Flint* Kaolin

Alex de Nazaré de Oliveira <sup>1,2,3</sup>, Erika Tallyta Leite Lima <sup>1,2</sup>, Eloisa Helena de Aguiar Andrade <sup>1,4</sup>, José Roberto Zamian <sup>1,2</sup>, Geraldo Narciso da Rocha Filho <sup>1,2</sup>, Carlos Emmerson Ferreira da Costa <sup>1,2</sup>, Luíza Helena de Oliveira Pires <sup>5</sup>, Rafael Luque <sup>6,\*</sup> and Luís Adriano Santos do Nascimento <sup>1,2,7,\*</sup>

<sup>1</sup> Graduation Program in Chemistry, Federal University of Pará, Augusto Corrêa Street, Guamá, Belém, PA 66075-110, Brazil; alexoliveiraquimica@hotmail.com (A.d.N.d.O.); erikatallyta@hotmail.com (E.T.L.L.); elena@ufpa.br (E.H.d.A.A.); zamian@ufpa.br (J.R.Z.); geraldonrf@gmail.com (G.N.d.R.F.); emmerson@ufpa.br (C.E.F.d.C.)

<sup>2</sup> Laboratory of Oils of the Amazon, Federal University of Pará, Perimetral Avenue, Guamá, Belém, PA 66075-750, Brazil

<sup>3</sup> Department of Exact and Technologic Sciences, Federal University of Amapá, Rod. Juscelino Kubitschek, km 02-Jardim Marco Zero, Macapá, AP 68903-419, Brazil

<sup>4</sup> Adolpho Ducke Laboratory, Botany Coordinating, Museu Paraense Emílio Goeldi, Perimetral Avenue, Terra Firme, Belém, PA 66077-830, Brazil

<sup>5</sup> Federal University of Pará, School of Application, Pará 66077-585, Brazil; lulenapires@hotmail.com

<sup>6</sup> Department of Organic Chemistry, Universidad de Córdoba, Ctra Nnal IV-A, Km 396, E14014 Córdoba, Spain

<sup>7</sup> Graduation Program in Biotechnology, Federal University of Pará, Augusto Corrêa Street, Guamá, Belém, PA 66075-110, Brazil

\* Correspondence: q62alsor@uco.es (R.L.); adrlui1@yahoo.com.br (L.A.S.d.N.); Tel.: +55-91-98171-4947

Received: 16 March 2020; Accepted: 23 April 2020; Published: 27 April 2020

**Abstract:** The present work was aimed to investigate the catalytic activity of a mesoporous catalyst synthesized from 3-mercaptopropyltrimethoxysilane (MPTS) functionalized Amazonian *flint* kaolin in the acetylation of eugenol with acetic anhydride. Materials were characterized by thermogravimetry (TGA), N<sub>2</sub> adsorption (BET), X-ray dispersive energy spectroscopy (EDX), X-ray diffraction (XRD), Fourier transform infrared spectroscopy (FTIR) and acid-base titration. The results presented proved the efficiency of *flint* kaolin as an alternative source in the preparation of mesoporous materials, since the material exhibited textural properties (specific surface area of 1071 m<sup>2</sup> g<sup>-1</sup>, pore volume of 1.05 cm<sup>3</sup> g<sup>-1</sup> and pore diameter of 3.85 nm) and structural properties ( $d_{100}$  = 4.35 nm,  $a_0$  = 5.06 nm and  $W_t$  = 1.21 nm) within the required and characteristic material standards. The catalyst with the total amount of acidic sites of 4.89 mmol H<sup>+</sup> g<sup>-1</sup> was efficient in converting 99.9% of eugenol (eugenol to acetic anhydride molar ratio of 1:5, 2% catalyst, temperature and reaction time 80 °C and 40 min reaction). In addition, the reused catalyst could be successfully recycled with 92% conversion activity under identical reaction conditions.

**Keywords:** eugenol; acetylation; *flint* kaolin; mesoporous aluminosilicate; functionalization; heterogeneous catalysis

## 1. Introduction

*Aedes aegypti* is an urban mosquito, which proliferates in areas of greater population density. Because it is typical of tropical and subtropical regions, it is considered a potential transmitter of the chikungunya, Zika virus (diseases that can generate other diseases, such as microcephaly and

Guillain–Barré), in addition to dengue and urban yellow fever. [1–4]. One of the main measures to prevent and combat *Aedes Aegypti* is with the use of insecticides and synthetic larvicides such as organochlorines, organophosphates, and others, to prevent the infestation of the adult and larval mosquitoes [1,3]. However, studies have shown that controlling the larval stage mosquito population is a more effective alternative than insecticide use in adult individuals [2,4–6]. For this reason, several researches are trying to develop new effective natural larvicides and insecticides, without toxic effect on man and the environment [2]. In this context, excellent results against *A. aegypti* larvae using eugenol and eugenyl acetate essential oils have been previously reported in the literature [2,4–6].

Eugenol is a natural product, belonging to the class of phenylpropanoids, found in greater quantity in the essential oil of cloves (*Eugenia Caryophyllata*) and exhibits a wide variety of biological, pharmacological and other applications, being a product of great commercial interest [4,5,7]. The interest of the scientific community for eugenol is justified by the fact that it is a reactant for synthesizing various natural and bioactive products through reactions such as acetylation reaction [4,8,9] or benzylation [10–12], within the scope of renewable resources. Eugenyl acetate obtained from eugenol, even in small amounts, has been reported as effective against *A. aegypti* mosquito larvae at development stage [2,4,6], being considered an efficient low cost natural larvicide [2–4,6,13].

The synthesis of eugenol esters often proceeds through homogeneous catalysis most often they are toxic or dangerous, such as mineral acids, chlorides, pyridine and their derivatives and more [2,14–16]. In addition to safety considerations, these technologies are also inefficient due to additional waste separation and treatment steps to isolate the product and thus are economically disadvantageous [10–12]. Although biocatalytic processes are alternative and environmentally friendly, to obtain the ester, in many cases it presents low capacity of reuse, making the process costly [5,17,18].

The development of solid catalysts is no longer seen simply in terms of cost and energy efficiency optimization, but as a clean technology [19]. The use of heterogeneous acid catalysts offers advantages over homogeneous ones such as solids recovery and recycling, as well as reducing environmental impacts [20–30]. Given the growing environmental problems, it is highly desirable to use heterogeneous catalysts in place of traditional homogeneous ones (corrosive, toxic and expensive) [10,17,24,31,32].

MCM-41 (Mobil Composition of Matter No. 41) mesoporous molecular sieves have been the most studied member of the M41S (Mobil 41 Synthesis) family. Their physical properties such as high pore volume and thermal stability, uniform pore diameters (from 1.5 to 10 nm) and large surface area [22,26,33–35] allow them to be applied as, heterogeneous catalytic supports and catalysts for several areas [24,28,33–35]. Generally, MCM-41 is synthesized using different sources of silica such as sodium silicate, tetraethylorthosilicate (TEOS), tetramethylammonium silicate (TMA-silicate) and the structure driver (cetyltrimethylammonium bromide, CTABr). However, these silica precursors have some disadvantages such as toxicity and the high cost of producing the material [36,37]. For economic and environmental reasons, the search for a synthesis procedure using alternative sources of silica, such as high purity kaolin, has been intensified aiming to obtain mesoporous material with a well-defined hexagonal arrangement [38–42]. Additionally, the waste from the kaolin processing [28] has proven to be an excellent source of silicon and aluminum for synthesis of highly ordered Al–MCM-41.

The process of transforming raw kaolin to a commercial product generates large amounts of waste that can have a great environmental impact. In this processing, a kaolinitic residue, kaolin *flint*, is generated with a high iron content and disposed in the mine shortly after exploration [25,43,44]. In order to minimize the environmental impacts caused by the residues of the kaolin industrial, our research group has been working on the use of this waste as raw material in the synthesis of catalytic materials and it has been shown to be quite viable because this material is composed essentially of kaolinite, the most common clay used as a source of Si and Al in the synthesis of materials. The use of kaolinitic tailings as raw material for catalyst synthesis [20,21,23,25], catalytic supports [22,27,28] and for mesoporous aluminosilicate synthesis [28] were reported to be efficient for the esterification of free fatty acids towards biofuel production.

*Flint* kaolin showed potential as a starting material for zeolite synthesis [43]. Recently, Oliveira et al. [24] demonstrated that it is possible to synthesize mesoporous aluminosilicate from this residue as an alternative source of silicon and aluminum, which enables it for various technological uses, including the synthesis of new catalytic materials, and which may lead to the development of specific integrated management projects. The synthesis of mesoporous aluminosilicates from low cost abundant natural clay minerals has been explored due to the similarities between their structural units and those of mesoporous materials [45,46].

As mentioned above, we have examples of work reporting the use of natural kaolinite as starting materials to synthesize Al-MCM-41. Generally, Al-MCM-41 exhibits a very high Si/Al molar ratio, and tends to show a decrease in the number of acid sites, thus reducing catalytic efficiency in reactions requiring a strong acid catalyst [24,28,38]. However, this problem can be solved by heteropoly acid impregnation [24,45] and anchoring of sulfonic groups [28] on the structure of Al-MCM-41 as an alternative method to obtain a high acid catalyst.

Sulfonic acids are organic compounds that have the functional group  $-\text{SO}_3\text{H}$  attached to a hydrocarbon radical [28]. Mesoporous molecular sieves functionalized with this acid group have increased hydrophobicity (inherent in the presence of the alkyl chain) due to the organosulfonic group anchored on the surface of the material, making them very efficient organic-inorganic hybrid catalysts [28,47–49]. Mercaptopropyltrimethoxysilane (MPTS) is commonly used to functionalize mesoporous materials [28,47,50,51], by covalently bonding to the silane groups on the aluminosilicate surface, the sulfonic form ( $-\text{SO}_3\text{H}$ ) being obtained only after an oxidation step of the  $-\text{SH}$  precursor (mercapto group) by an oxidizing agent such as hydrogen peroxide [28,50].

Herein is an extension of our group's previous work, in which Lima and colleagues [28] synthesized Al-MCM-41 aluminosilicate from kaolinitic residue from the kaolin processing process and functionalized with sulfonic groups to obtain a very efficient catalyst for the conversion of free fatty acids into biodiesel. In another study, Oliveira et al. [24] synthesized a very active heterogeneous 10HPMo/AlSiM acid catalyst from kaolin *flint* for the reaction of eugenol acetylation with acetic anhydride. It was considered interesting to use a mesoporous aluminosilicate support synthesized from another available low cost kaolinitic tailings in the Amazon region, the *flint* kaolin [24]. In the present work, for the first time, we report the synthesis and characterization of mesoporous aluminosilicate (AlSiM) anchored MPTS from *flint* kaolin, as well as the use of this type of material as catalyst for the eugenol and acetic anhydride acetylation reaction for production eugenyl acetate, which can be used as a natural larvicide. Catalytic activity was evaluated for the esterification of eugenol and acetic anhydride as model substrates studying the effect of various reaction parameters, such as catalyst concentration, eugenol/acetic anhydride molar ratio, time and temperature, and the catalyst was regenerated up to five cycles. A kinetic study was also carried out and it was found that the acetylation reaction follows a first order reaction.

## 2. Results and Discussion

### 2.1. X-ray Fluorescence (XRF) Studies

Once the stoichiometric calculations of reagents required to form AlSiM is influenced by the percentage of silicon [52], it is fundamental to know about the chemical composition of the silica precursors. Table 1 shows the XRF (EDX; EDX-700, SHIMADZU, Kyoto, Japan) results. The amounts of  $\text{SiO}_2$ ,  $\text{Al}_2\text{O}_3$  and  $\text{H}_2\text{O}$  present in the *flint* kaolin (KF) are almost the same as the theoretical values obtained for kaolinite [21,25,43,44]. The values found for  $\text{TiO}_2$  and  $\text{Fe}_2\text{O}_3$  in KF, are mainly due to the greater presence of anatase ( $\text{TiO}_2$ ) and hematite ( $\text{Fe}_2\text{O}_3$ ). However, the high percentage of iron in KF may have occurred due to the isomorphic substitution of  $\text{Al}^{3+}$  by  $\text{Fe}^{3+}$  on the kaolinite octahedral sheet. [25,43,44]. Due to the dealumination process caused by acid leaching of metakaolin *flint* (MF), in KF there is a mass a Si/Al ratio close to 1, in metakaolin *flint* leached (MFL) this ratio rises to 13 [28,38], while in the synthesized AlSiM it showed a Si/Al of 23 much higher than its precursor MFL.

The data in Table 1 also shows the presence of  $\text{SO}_3$  for (3) $\text{SO}_3\text{H}/\text{AlSiM}$  and (5) $\text{SO}_3\text{H}/\text{AlSiM}$ , indicating that sulfonic groups are present in the AlSiM structure [28,50]

**Table 1.** XRF analysis results of the raw material and samples prepared.

Samples	SiO <sub>2</sub>	Al <sub>2</sub> O <sub>3</sub>	TiO <sub>2</sub>	Fe <sub>2</sub> O <sub>3</sub>	SO <sub>3</sub>	LF <sup>a</sup>	Si/Al
K <sup>b</sup>	46.54	39.50				13.96	1
KF	42.30	38.29	3.20	2.92		13.29	1
MF	49.64	37.92	2.50	2.78		1.25	1
MFL	73.98	4.74	3.71	1.62		15.89	13
AlSiM	86.72	3.21	3.52	1.10		5.23	23
(3)SO <sub>3</sub> H/AlSiM	69.09	1.71	2.16	0.26	8.70	18.08	34
(5)SO <sub>3</sub> H/AlSiM	61.39	1.55	1.83	0.10	11.06	24.07	34

<sup>a</sup> LF = loss on ignition; <sup>b</sup> K = theoretical kaolinite [21,25,43,44]; (3 or 5) SO<sub>3</sub>H/AlSiM denotes (3 or 5 mmol) mercaptopropyltrimethoxysilane (MPT) functionalized in AlSiM.

## 2.2. XRD Analysis

In the diffractograms (Bruker D8 Advance; Bruker Corp, Billerica, MA, EUA) presented in Figure 1a, For the KF sample we identify the main mineralogical components of the material where kaolinite (K) presents the highest intensity peak. This material also has low intensity components such as: quartz (Q), anatase (A) and hematite (H). These results are in agreement with the mineralogical compositions of the researched literature [25,43,44]. For the calcined sample (MF) at 750 °C for 2 h (Figure 1a), absence of characteristic peaks for kaolinite (close to  $2\theta = 12$  e  $24^\circ$ ). The lack of these characteristic peaks is due to the dehydroxylation of the Al(OH)<sub>6</sub> octahedral layer which becomes coordinated Al tetra and penta units during heat treatment, which makes this material more susceptible to acid leaching [21–23,25,44]. For leached metakaolin samples, no significant changes were observed in relation to their metakaolinitic *flint* precursor (MF).

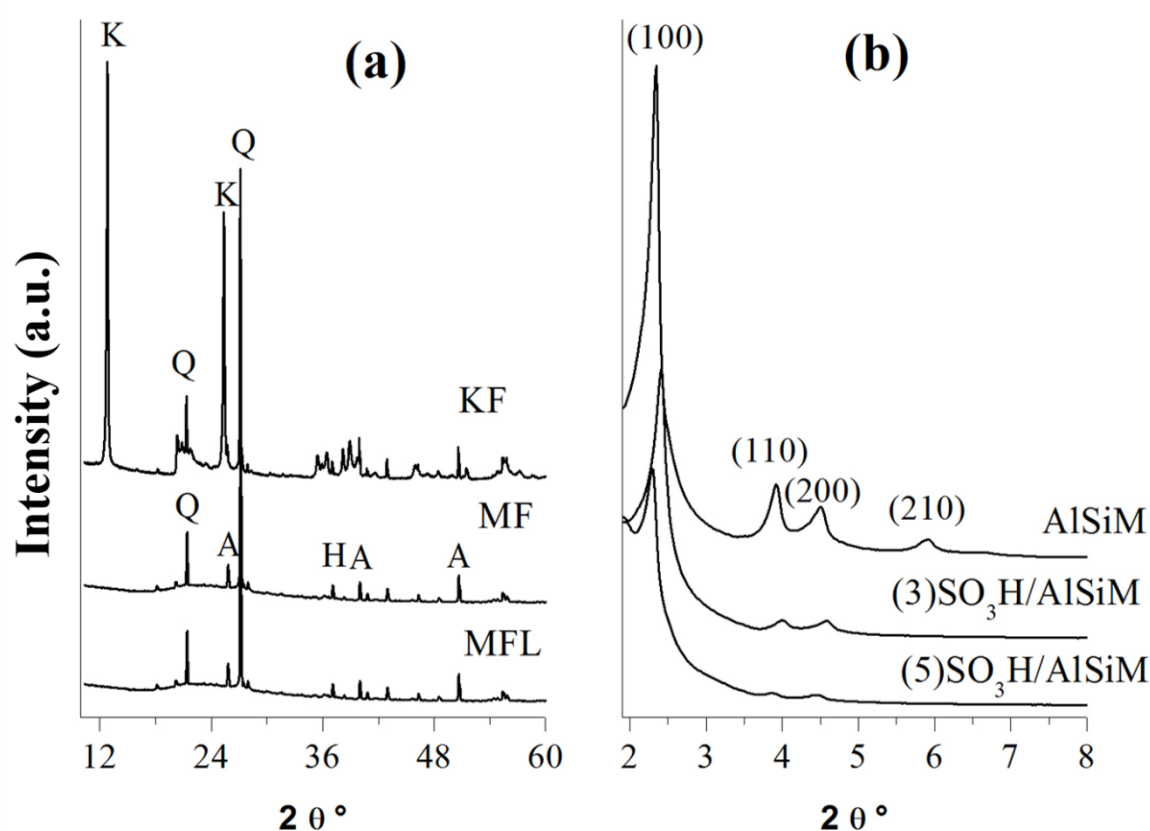


**Figure 1.** X-ray diffraction patterns: (a) *flint* kaolin (KF), metakaolin *flint* (MF), metakaolin *flint* leached (MFL), K = kaolinite, Q = quartz, A = anatase, H = hematite. and (b) aluminosilicates calcined (AlSiM) and functionalized with sulfonic group, (3)SO<sub>3</sub>H/AlSiM and (5)SO<sub>3</sub>H/AlSiM.

XRD patterns of AlSiM exhibited four peaks (1 intense and 3 weak) at low  $2\theta$  values that can be indexed as (100), (110), (200) and (210) reflections characteristics of mesoporous materials with hexagonal arrangement of their cylindrical channels [40–42]; even after calcination (540 °C) there was no collapse of the structure. The Si/Al molar ratio of AlSiM obtained, which was close to 23, is suitable to form mesoporous silicas with well-defined structures, which have a high silicon content [28,38]. These results according with data found in literature, proving well-ordered formation of the structures with Si/Al molar ratio equal to 13.8 [53], Si/Al of 20 [28], Si/Al of 29.3 [42] and Si/Al of 32.1 [38].

For samples (3 or 5) SO<sub>3</sub>H/AlSiM it is possible to observe characteristic peaks of the hexagonal system. As the AlSiM anchored MPTS content increased, it caused changes in the porous structure of the support as the four reflections widened and the peaks shifted to greater angles. This shift can be explained by a slight decrease in pore size resulting from the insertion of the sulfonic group into the linear pores of the AlSiM peak  $d_{100}$  becomes less intense and broad as reflections (110, 200 and 210) follow the same trend and disappear [28,48]. The absence of reflections at higher angles ( $>2\theta$ ) is an indication that the samples of (3 or 5)SO<sub>3</sub>H/AlSiM have a structure with low structural order compared to AlSiM, however, there is a preserved hexagonal arrangement, which can be observed by the first  $d_{100}$  reflection plane even after functionalization with MPTS [28,48,50].

Table 2 shows the XRD data of the aluminosilicate samples studied from the reflection (100) obtained from each material, which correspond to the standards found in the literature [28,39–42,45,54]. The interplanar spacings ( $d_{100}$ ) and the network parameters ( $a_0$ ) calculated from the reflection (100) are also in good correspondence with literature data [39–42,45,54].

**Table 2.** Textural and structural characteristics.

Samples	Textural Property			Structural Property		
	SSA (m <sup>2</sup> g <sup>-1</sup> ) <sup>a</sup>	V <sub>p</sub> (cm <sup>3</sup> g <sup>-1</sup> ) <sup>b</sup>	D <sub>p</sub> (nm) <sup>c</sup>	$d_{100}$ (nm) <sup>d</sup>	$a_0$ (nm) <sup>e</sup>	W <sub>t</sub> (nm) <sup>f</sup>
KF	8.9	0.05	32.20	-	-	-
MF	9.78	0.05	31.11	-	-	-
MFL	433	0.56	1.20	-	-	-
AlSiM	1071	1.05	3.85	4.35	5.06	1.21
(3)SO <sub>3</sub> H/AlSiM	998	0.78	3.25	4.07	4.70	1.45
(5)SO <sub>3</sub> H/AlSiM	869	0.65	3.01	4.04	4.67	1.66

<sup>a</sup> SSA = specific surface area (BET method); <sup>b</sup> V<sub>p</sub> = pore volume (BJH method); <sup>c</sup> D<sub>p</sub> = pore diameter (BJH method); <sup>d</sup>  $d_{100}$  = interplanar spacing (100) ( $d_{100} = \lambda \text{CuK}\alpha / \sin\theta$ ) [28,34]; <sup>e</sup>  $a_0$  = hexagonal unit cell parameter ( $2d_{100}/\sqrt{3}$ ) [28,34]; <sup>f</sup> W<sub>t</sub> = mesoporous wall thickness ( $W_t = a_0 - D_p$ ) [28,34].

### 2.3. Nitrogen Physisorption Experiments

The dehydroxylation of kaolinite by calcination led to the formation of metakaolin, considerably increasing SSA and V<sub>p</sub> after acid leaching (Figure 2a and Table 1) (Micromeritics TriStar II model 3020 V1.03 apparatus (Micromeritics, Norcross, GA, USA). The MFL (433 m<sup>2</sup> g<sup>-1</sup>) after the dealumination process (Al<sub>2</sub>O<sub>3</sub>~88%, Table 1) had its SSA increased by approximately 43 times compared with its precursor (MF, 9.78 m<sup>2</sup> g<sup>-1</sup>).

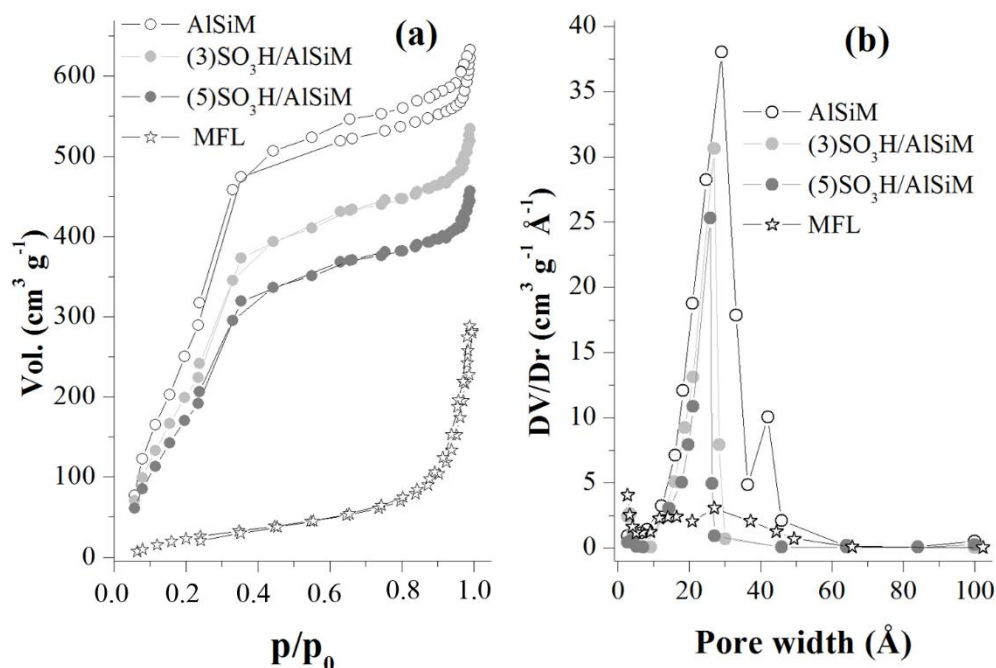


**Figure 2.** N<sub>2</sub> physisorption isotherms (a) and pore size distribution curves (b) of MFL, AlSiM and (3 or 5)SO<sub>3</sub>H/AlSiM.

The isothermal forms of the four samples were completely different. MFL isotherm is a mixture of type II and IV according to Du and Yang [42], with an isotherm-like initial portion type I and a hysteresis loop mixture of H3 and H4, indicative of narrow slit pores. The preparation of porous material (MFL) from the MF by leaching involved the removal of part of the Al<sub>2</sub>O<sub>3</sub> (Table 1) of MF by acid treatment, leaving pores within the structure of the MFL [40–42].

N<sub>2</sub> physisorption isotherms and pore size distribution of AlSiM and (3 or 5)SO<sub>3</sub>H/AlSiM samples (Figure 2a,b) are all type IV according to the IUPAC type IV classification [55,56], an indicative of the formation of mesoporous material which structures were not compromised, even after functionalization, a behavior similar to those reported in the literature for materials of this type [28,33–35], with characteristic hysteresis cycle of uniform mesoporous material, corresponding to mesoporous materials obtained from metakaolin [39,41,42].

Figure 2a shows three distinct regions at low relative pressures. At  $p/p_0 < 0.2$ , N<sub>2</sub> adsorption occurs in monolayer and multilayer on the pore walls. Then, at average relative pressures, between  $0.2 < p/p_0 < 0.3$ , there is a strong increase in N<sub>2</sub> adsorption that is caused by capillary condensation of nitrogen inside the primary mesopores [39,42]. The formation of a hysteresis loop in  $p/p_0$  equal to 0.3 is observed and results from an abrupt increase in the amount of adsorbed N<sub>2</sub>, due to capillary condensation inside the mesoporous material [41]. With the filling of all primary mesopores by N<sub>2</sub>, the third region starts in  $p/p_0 > 0.3$ , where the slope of the curve decreases tending to a plateau, which characterizes the adsorption in multilayers on the external surface of the solid [39,42]. Isotherms of mesoporous materials with a certain Al content, generally show a strong increase in the curve in  $p/p_0 > 0.9$ , which is related capillary condensation in secondary mesopores due to the voids formed by crystalline aggregates in the hexagonal structure of the materials [39,42].

The pore size distribution shown in Figure 2b shows a narrow main peak centered at 2.8 nm, showing the presence of uniform mesopores. This result corroborates with that obtained by the XRD analysis (see Figure 1b), which revealed the formation of a highly ordered structure of the mesoporous molecular sieve (AlSiM) obtained in this work. The mesoporous material developed from KF as a source of Si and Al showed physical properties quite similar to the materials prepared using commercial metakaolin [39–42] or synthetic silica [22,33,34,57–60].

From the literature data [24,28,38–42] and the results of the textural analyzes obtained for the AlSiM synthesized in this work, it is possible to state that KF can be used as a low-cost silica source

for the synthesis of mesoporous molecular sieves with uniform pores and with regular hexagonal arrangement.

Samples (3 or 5)SO<sub>3</sub>H/AlSiM showed isothermal forms of N<sub>2</sub> physisorption analogous to AlSiM, with capillary condensation within the mesoporous close to the relative pressure range between  $0.2 < p/p_0 < 0.3$ . However, the adsorbed N<sub>2</sub> volume decreased with increasing MPTS content due to the structural disorder of the samples (Figure 1b). Consequently, SSA decreased from 1071 m<sup>2</sup> g<sup>−1</sup> (AlSiM) for 869 m<sup>2</sup> g<sup>−1</sup> (5)SO<sub>3</sub>H/AlSiM, for the sample with the highest mmol of MPTS. Variation in MPTS content in the anchoring process did not significantly affect the average pore diameter but reduced the pore volume and increased the wall thickness of the samples (Table 2). The data of N<sub>2</sub> physisorption for these materials is in accordance with other mesoporous silicates functionalized with sulfonic groups [28,50,61]. Textural properties, such as SSA, V<sub>p</sub>, and D<sub>p</sub>, derived from N<sub>2</sub> physisorption measures are showed in Table 2. N<sub>2</sub> physisorption and XRD studies revealed that MPTS functionalization did not affect the mesoporous structures of these materials (Figures 1b,e and 2a).

#### 2.4. Fourier Transform Infrared Spectroscopy (FTIR) Experiments

AlSiM and (3 or 5)SO<sub>3</sub>H/AlSiM FTIR spectra are shown in Figure 3. AlSiM FTIR (Shimadzu, Kyoto, Japan) spectrum show a broadband between 1228–1060 cm<sup>−1</sup> (asymmetrical stretching elongation vibrations O–Si–O). Also in the AlSiM spectrum, bands are observed at 967, 795 and 460 cm<sup>−1</sup>, which correspond to the stretching vibration of silanols (Si–OH, tetraordinated to silicon), angular deformation of the Si–O–Al bonds [39,42] and vibrational deformation of the tetrahedral bonds between Si–O–Si [48], respectively, after calcination of material these bands are also lightly shifted to higher frequencies [39,42].

FTIR analysis shows variations in spectra caused by support functionalization by sulfonic groups. Figure 3 of all samples present bands around 3447 and 1633 cm<sup>−1</sup> that correspond to water adsorption by silanol groups located on the surface of the mesoporous material and the vibrational deformation of the adsorbed water, respectively [37–39]. The significant band at 2933 cm<sup>−1</sup> is induced by symmetrical and asymmetrical vibrations of –CH<sub>2</sub> present on the surface of the catalysts, showing that the MPTS reacted successfully with silanol groups and is covalently attached to the surface of the AlSiM [62]. The O–H strain vibration near 1633 cm<sup>−1</sup> can be seen in all samples [48]. The band near 595 cm<sup>−1</sup> may be due to C–S stretch vibration [61]. However, in the AlSiM sample, bands close to 2395 cm<sup>−1</sup> could be observed which could also correspond to the symmetrical and asymmetric stretching of the C–O bond in the CO<sub>2</sub> molecule. These spectral results are quite consistent with those observed in the literature [61]. In the spectral range between 1300 e 1500 cm<sup>−1</sup> of samples (3 or 5)SO<sub>3</sub>H/AlSiM compared to the AlSiM matrix, absorption band around 1408 cm<sup>−1</sup> is associated with the asymmetric and symmetrical stretching signals of O=S=O bonds of sulfonic groups [48,63]. The existence of the sulfonic acid group (SO<sub>3</sub>H) in the samples (3 or 5)SO<sub>3</sub>H/AlSiM was confirmed by the presence of an intense and wide absorption band at 3458 cm<sup>−1</sup>, which corresponds to the vibration of the S–OH bond stretch, in addition to the 1408 cm<sup>−1</sup> band attributed to asymmetric and symmetrical vibration connections (O=S=O), confirming the covalent anchoring of (SO<sub>3</sub>H) to the surface of AlSiM [62,63] These results reveal that the sulfonic acid group was successfully anchored on the support surface, corroborating the data obtained by the XRF technique regarding the chemical composition (Table 1).



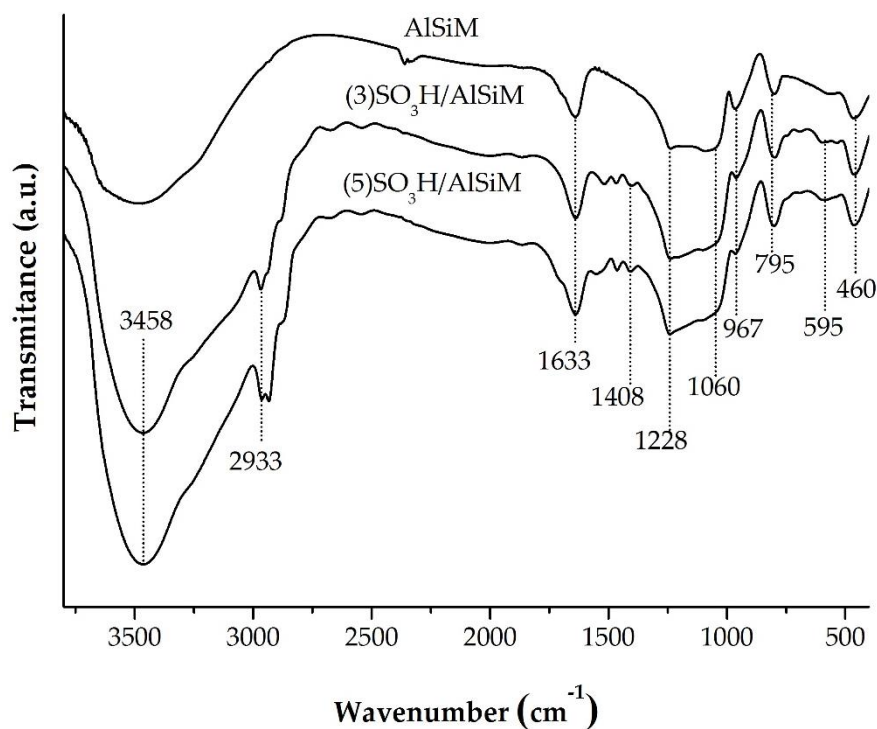


**Figure 3.** FTIR spectra of samples AlSiM e (3 or 5)SO<sub>3</sub>H/AlSiM.

### 2.5. Thermal Analysis (TGA/DTG) Results

The existence of organosulfonic groups was monitored based on TGA/DTG (Shimadzu, Kyoto, Japan) analysis. The thermogravimetric analysis curves for AlSiM, (3 or 5)SO<sub>3</sub>H/AlSiM are presented in Figure 4. Mass losses are more clearly identified by the DTG as it occurs on all TGA curves. The data obtained by TGA/DTG are summarized in Table 3, confirming mass losses in certain temperature ranges for both pure and functionalized AlSiM. In all samples an initial mass loss of 25 to 200 °C is observed, which many authors attributed to physically adsorbed water thermosorption on the surface of the materials [48,61,63].

The anchorage of organosulfonic groups in the AlSiM structure was followed by TGA analysis as shown in Figure 4. In Figure 4 we can see significant losses before 200 °C due to evaporation of water adsorbed some release of SO<sub>2</sub> from sulfonic acid groups (propyl-SH and propyl-SO<sub>3</sub>, respectively) [49,61,64]. Two mass losses were observed in the range 200–470 °C, is attributed to the decomposition of organic matter, degradation of propyl groups present in the catalysts [49,61,64], towards higher temperatures is seen at the peak of organic matter elimination at 380 °C shown by the DTG curve. The final mass loss (between 500 to 900 °C) can be attributed to the higher thermal stability of the oxidized propyl sulfonic group [50] and the decomposition of residual organic groups and the condensation of neighboring silanol groups forming siloxane bridges, releasing water molecules [48,61,63]. The XRF analysis (Table 1) and FTIR (Figure 3) of functionalized material corroborate the results of the TGA, and the sample with the highest MTPS load was the sample with the highest mass loss, which is naturally caused by the larger amount of functionalized material.



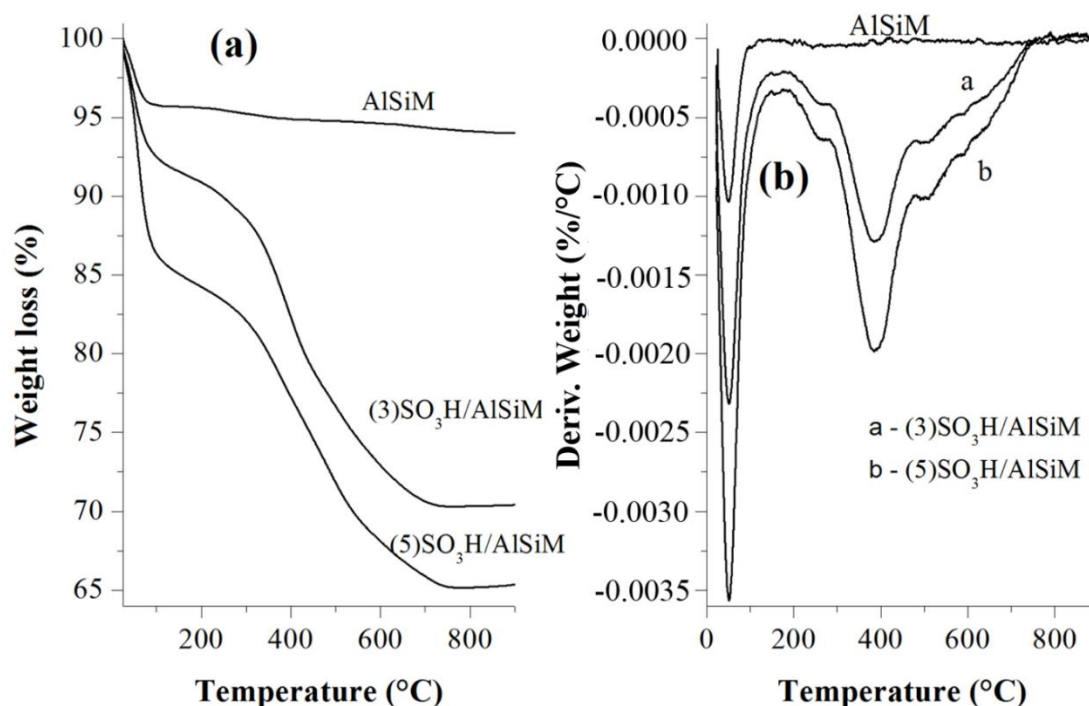


**Figure 4.** Thermal stability determined by TGA/DTG of AlSiM and (3 or 5)SO<sub>3</sub>H/AlSiM (a) TGA and (b) DTG.

**Table 3.** Mass loss (%) with respective temperature ranges.

Samples	Mass Losses (%)			Total
	I (T < 200 °C)	II(200–430 °C)	III(T > 430 °C)	
AlSiM	3.96	0.99	0.80	5.23
(3)SO <sub>3</sub> H/AlSiM	8.23	6.71	5.75	20.69
(5)SO <sub>3</sub> H/AlSiM	12.65	8.09	6.55	27.29

## 2.6. Surface Acidity

The surface acidity of the AlSiM and functionalized (3 or 5)SO<sub>3</sub>H/AlSiM solids were evaluated by acid–base titration [22,23,27]. Another way to evaluate the acidity of the materials was by means of FTIR methodologies and TGA/DTG technique after adsorption of pyridine as probe molecule on the material, which allows to characterize heterogeneous catalysts and to quantify acid sites efficiently [21,23,25,27].

Considering that the catalysts (3 or 5)SO<sub>3</sub>H/AlSiM were the most active in the preliminary reaction studied, the number of acid sites obtained for these materials was due to the consumption of hydroxyls (titration) and adsorption of pyridine [21–23,25,27]. Table 4 shows the total hydroxyls and pyridines consumed, which indicates that all catalysts had more acid sites when compared to their support (AlSiM), because the number of acid sites (3 and 5 mmol) of MPT are present in the support structure (Table 1).

From Figure 5, TGA/DTG curves revealed that (3 or 5) SO<sub>3</sub>H/AlSiM with adsorbed pyridine (Py) lost more mass than samples without adsorbed pyridine. In the range between 150 and 250 °C, the samples (3 or 5)SO<sub>3</sub>H/AlSiM Py have losses that may be related to water and physically adsorbed pyridine, while there is a continuous loss that is attributed to chemically adsorbed pyridine above 250 °C. The methodology described by Nascimento et al. [21,25] Using TGA/DTG

curves after pyridine adsorption was used to define the acidity and the number of acid sites of the catalysts.

**Table 4.** Evaluation of acidity of the prepared materials and conversion of eugenol.

Amostras	(mmol H <sup>+</sup> g <sup>-1</sup> ) <sup>a</sup>	(μmol g <sup>-1</sup> ) <sup>b</sup>	Conv. (%) <sup>c</sup>
AlSiM	1.31		27
(3)SO <sub>3</sub> H/AlSiM	5.93	295	97
(5)SO <sub>3</sub> H/AlSiM	4.89	236	89

<sup>a</sup> Total surface acidity by titration [22,23]; <sup>b</sup> mole of pyridine by TGA/DTG analysis [25]; <sup>c</sup> conversion of eugenol (EugOH: AA molar ratio = 1:5, 2% catalyst, 80 °C, 30 min).

In Figure 5, It was observed that the acidity of each material resulted directly from the number of mmol of MPTS functionalized in the support. Analyzing the Table 4, it was noted that the sample with lower MPTS content presented higher number of acid sites, (3)SO<sub>3</sub>H/AlSiM (295 μmol g<sup>-1</sup>) > (5)SO<sub>3</sub>H/AlSiM (236 μmol g<sup>-1</sup>), which may be justified by the greater accessibility of pyridine molecules to the acid sites of the functionalized material that had the highest textural properties (Table 2).

The concentrations of acidic sites measured by titration with NaOH were higher than those measured with pyridine. This may have been caused by the deposition of acidic sites (Al<sup>3+</sup> or –SO<sub>3</sub>H) on the pore surface of the material when the pyridine was adsorbed. Because pyridine is a bulky molecule, it may have caused a local blockage in the pore channels, making it difficult for other pyridine molecules to diffuse to the active sites present inside the solid. This difficulty in accessing pyridine to acidic sites significantly reduces the acidity values of the material. This relationship has already been reported in the literature in studies involving samples impregnated with pyridine and ammonia [65].

In FTIR spectra of the materials treated with pyridine (Figure 5b), bands related to pyridine physisorption were observed in 1637 and 1542 cm<sup>-1</sup>, referring to the Brønsted acid sites; in 1577, 1533, 1447 and 1440 cm<sup>-1</sup>, indicating the presence of Lewis acid sites; and in 1437 cm<sup>-1</sup>, which refer to the acid sites of Brønsted and Lewis. In (3)SO<sub>3</sub>H/AlSiM and (5)SO<sub>3</sub>H/AlSiM samples, the generation of Lewis acid sites is possibly due to aluminum [23,25] present in the support (AlSiM) and Brønsted acid sites may be due to the presence of sulfonic acid group (SO<sub>3</sub>H) [63], attested by the XRF technique (Table 1). Thus, the catalysts consist of Lewis acid sites and Brønsted acid site. This profile is in line with that presented by other mesoporous materials with sulfonic groups [63].

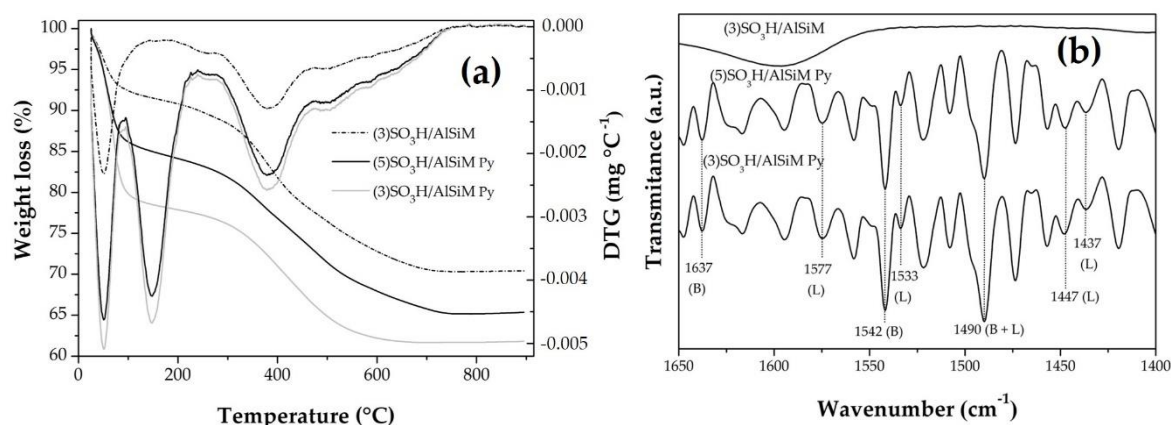


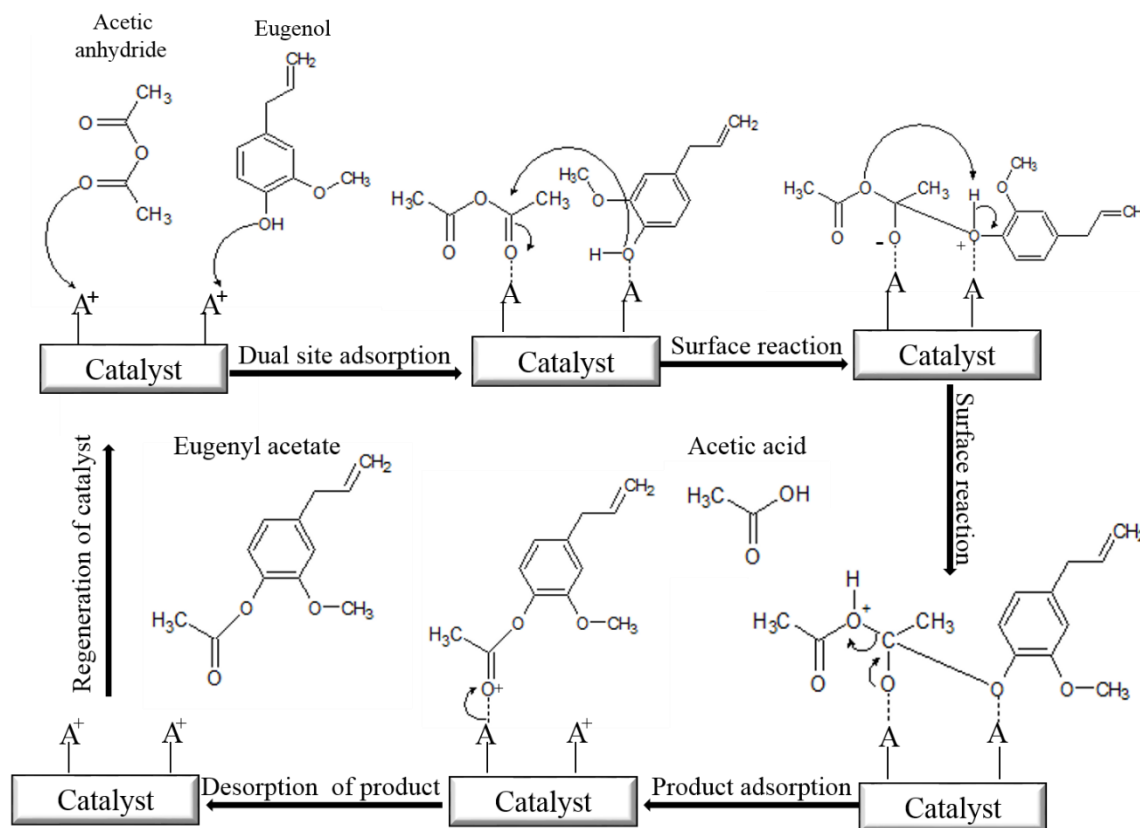
**Figure 5.** TGA/DTG curves (a) and FTIR spectra (b) of catalysts without/with adsorbed pyridine: (3) SO<sub>3</sub>H/AlSiM and (3 or 5)SO<sub>3</sub>H/AlSiM Py.

The results indicated the presence of substantial surface acidity in the catalysts and confirmed by FTIR spectra, and they clearly showed the presence of higher number of acid sites in (3) SO<sub>3</sub>H/AlSiM due to higher SSA. Thus, the total acid sites are more dispersed by generating more accessible acid sites, compared to (5) SO<sub>3</sub>H/AlSiM with 236 μmol g<sup>-1</sup> acid sites distributed in smaller SSA (869 m<sup>2</sup> g<sup>-1</sup>).

The acidity of the catalysts was evaluated in preliminary experiments on the eugenol acetylation reaction and these results are presented in Table 4. In the control tests, the conversion rate achieved over AlSiM was similar to the blank reaction (24% in 30 min). However, only the reactions catalyzed by the functionalized materials, (3) SO<sub>3</sub>H/AlSiM > (5)SO<sub>3</sub>H/AlSiM, showed significantly higher conversion rates than those obtained from the control experiments.

The observed trend (3) SO<sub>3</sub>H/AlSiM > (5)SO<sub>3</sub>H/AlSiM demonstrates the importance of catalytic acid site density and textural properties such as high SSA as well as V<sub>P</sub> and D<sub>P</sub> of the present catalyst pores play an important role in the diffusion of bulky molecules. such as eugenol and eugenol ester on the catalyst surface [10,66]. In the present case both catalysts have pore diameters of 3.25 nm ((3)SO<sub>3</sub>H/AlSiM), 3.01 nm ((5)SO<sub>3</sub>H/AlSiM), respectively, much larger than the maximum molecular size of the pore eugenol (~0.92 nm) and eugenyl acetate (~1.2 nm) (derived from Gaussian software as shown in Scheme 3). Therefore, there is sufficient space for diffusion of both reagents and products into the pores of both catalysts.

Low acid site concentration, together with lower SSA (869 m<sup>2</sup> g<sup>-1</sup>) and V<sub>P</sub> (0.65 nm), are likely to be the most likely contributing factors to the low activity of (5)SO<sub>3</sub>H/AlSiM. Although (5) SO<sub>3</sub>H/AlSiM has more organic groups (–SO<sub>3</sub>) in its structure confirmed by XRF (Table 1) and TGA (Figure 4) analyzes, it appears that the active sites were less accessible during both acidity study. as in catalytic testing (Table 4). However, the high catalytic activity of (3)SO<sub>3</sub>H/AlSiM can be attributed to the presence of large SSA (998 m<sup>2</sup> g<sup>-1</sup>) and V<sub>P</sub> (0.78 cm<sup>3</sup> g<sup>-1</sup>), respectively, which contributed to both diffusion of these interacting large molecules. on the reagent-accessible active sites during the surface reaction. This facilitated the adsorption of polar substrates, such as eugenol and acetic anhydride, on the catalyst surface (Scheme 1) [10,67]. In addition, as eugenyl acetate is less hydrophilic than eugenol and acetic anhydride, (3)SO<sub>3</sub>H/AlSiM showed a high tendency to adsorb these molecules and consequently showed higher product formation after prolonged reaction times [10,24,67].



A<sup>+</sup> = Bronsted and Lewis acid sites

**Scheme 1.** Proposed mechanism for eugenol acetylation reaction on solid acid catalyst adaptation [10,24].

Overall, the results showed a good correlation with the effects of catalytic acid site density, textural properties and reagent molecule dimensions on catalyst reactivity, which are in good agreement with the trends found in the literature [10,17,31,32]. Effectively, (3)SO<sub>3</sub>H/AlSiM has demonstrated activity that matches resins, *Amberlyst A-21* (95%) [32], *Amberlite XAD-16* (98%) [31] and *Lewatit® GF 101* (100%) [17]. As these results were satisfactory, (3) SO<sub>3</sub>H/AlSiM was appointed for further investigation of various reaction parameters, such as the molar relationship between eugenol and acetic anhydride, catalyst amount, temperature and time and catalyst reuse to optimize reaction variables to achieve maximum eugenol conversion (confirmed by FTIR and GC-MS see supplementary material).

### 2.7. Eugenol Acetylation Reaction Mechanism with Acetic Anhydride

The eugenol (EugOH) (99% Aldrich, San Luis, Missouri, EUA) derivative ester was synthesized using acetic anhydride (AA) (Nuclear, São Paulo, SP–Brazil) in acid-solid catalyzed reactions following literature procedures [31,32]. Acetylation of eugenol with acetic anhydride is a limited equilibrium reaction. In order to overcome balance limitation, eugenol acetylation is usually performed by taking excess acetic anhydride to favor the direct reaction [5,67]. The mechanism is shown in Scheme 1.

A simple explanation for elucidating the pathway of the acetylation reaction mechanism on the acid catalyst surface [10,24] is shown in Scheme 1. Assuming the reaction takes place by the Langmuir–Hinshelwood–Hougen–Watson mechanism, where adsorbed reagents interact with acidic sites on the catalyst surface to form the products [10,24].

First, both reagents are adsorbed to the active sites (Brønsted and Lewis acids) of the catalyst [10,67]. In the next two steps, the surface reaction proceeds with the formation of the carbocation (electrophile) that is attacked by the nucleophile (eugenol) generating a protonated tetrahedral intermediate [68,69]. The transfer and rearrangement of protons (H<sup>+</sup>) from hydroxyl (eugenol) to carbonyl oxygen (acetic anhydride) occurs in this intermediate which results in the formation of a rearranged tetrahedral intermediate. The subsequent stage takes place with the acetic acid leaving the tetrahedral intermediate, obtaining protonated eugenyl acetate [10,24]. Thus, the tetrahedral intermediate desorption (electron transfer from the catalyst acid site to the carbonyl oxygen, leading to bond disruption) and simultaneously the deprotonation of the ester and catalyst regeneration are initiated [10,70].

### 2.8. Effect of Temperature

The effect of reaction temperature was studied in the temperature range of 50 to 100 °C (Figure 6). A gradual increase in eugenol conversion from 85% to 99.3% was observed increasing the temperature from 50 to 80 °C after 40 min. As reported by Laroque et al. [31] and Santos et al. [67] at higher temperatures improves eugenol solubility and miscibility with anhydride, facilitating protonation of the acetic anhydride carbonyl group and eugenol nucleophilic attack on carbocation, resulting in higher eugenol conversion (Scheme 1). Compared to different reports, Lerin et al. [32], using *Amberlyst A-21* obtained 95% eugenol conversion at 95 °C. Another material known as zirconia dioxide (UDCaT-5) recorded 90% eugenol conversion at 110 °C Yadav [10]. As the boiling point of both eugenol and acetic anhydride is greater than 100 °C, and all reactions have been studied up to 100 °C, possibly there was no vapor loss during the liquid phase reaction. Hence, the temperature 80 °C was selected for acetylation for eugenol.

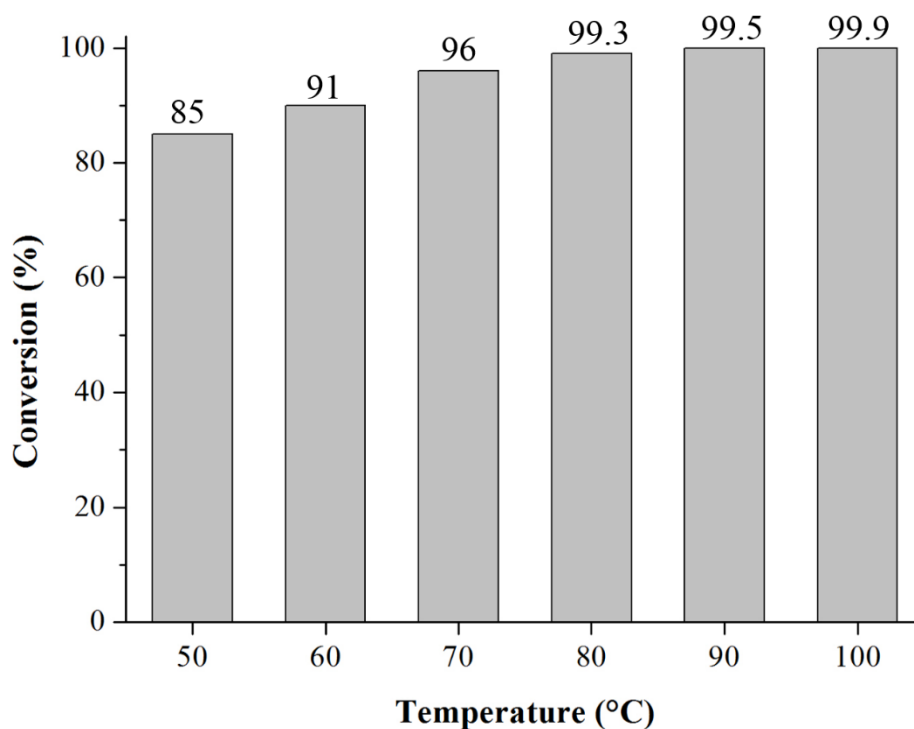


**Figure 6.** Percentage conversions of eugenyl acetate varying the reaction temperature. Reaction conditions: eugenol: acetic anhydride (1:5), reaction time 40 min and 2% catalyst.

### 2.9. Amount of Catalyst

Reactions without catalyst were performed, once the autocatalysis can occur according to the mechanisms for the reaction studied [4,17], and the result for self-conversion was not higher than 24% (Figure 7). This reveals that the high activity of the catalyst in the reaction rate is directly proportional to the catalyst load based on the total reaction volume [10,17,31,71,72].

Figure 7 shows the change in conversion (%) with the amount of catalyst charged during eugenol acetylation. The effect of the amount of catalyst was investigated by percent dosing from 1 to 4% mass (based on eugenol mass) of catalyst (3)  $\text{SO}_3\text{H}/\text{AlSiM}$ . Eugenol conversion has been observed to increase from 75% to its final value of 98% as catalyst dosage increases from 1% to 2%. However, this increase in eugenol conversion is expected due to the availability of more active sites that facilitate the acetylation reaction [10,31,32]. An additional increase in catalyst amounts resulted in not very appreciable changes in conversion, indicating that 2% catalyst represents the appropriate level of active sites for eugenol acetylation and that the equilibrium of the reaction is achieved.

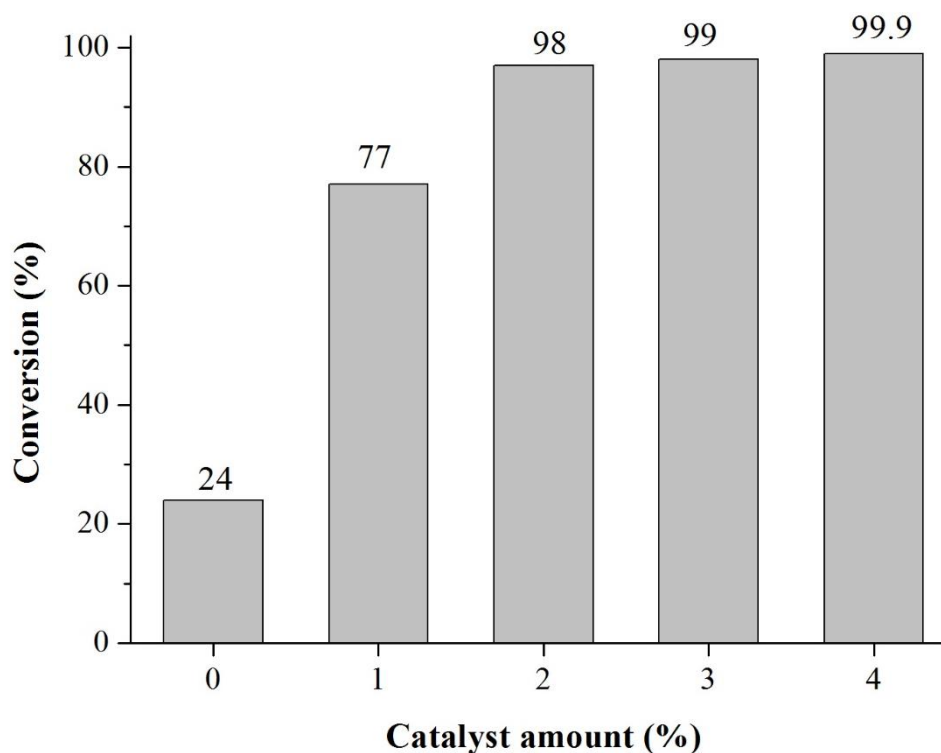


**Figure 7.** Percentage conversions of eugenyl acetate with different amount of catalyst. Reaction conditions: eugenol: acetic anhydride (1:5), reaction temperature 80 °C and reaction time 40 min.

#### 2.10. Molar Ratio between Reagents

The reaction was studied with a molar ratio of eugenol to acetic anhydride from 1:2 to 1:7 over a 2% catalyst amount (relative to eugenol) at 80 °C for 40 min (Figure 8). The results showed a 61% conversion of eugenol with a 1:2 molar ratio of eugenol to acetic anhydride, which increased to 98% with the successive increase of the eugenol to acetic anhydride ratio to 1:5. However, by further increasing the eugenol to acetic anhydride ratio to 1:7, an almost similar conversion of eugenol (99%) was observed. Therefore, the eugenol to acetic anhydride ratio of 1:5 was selected for further studies.

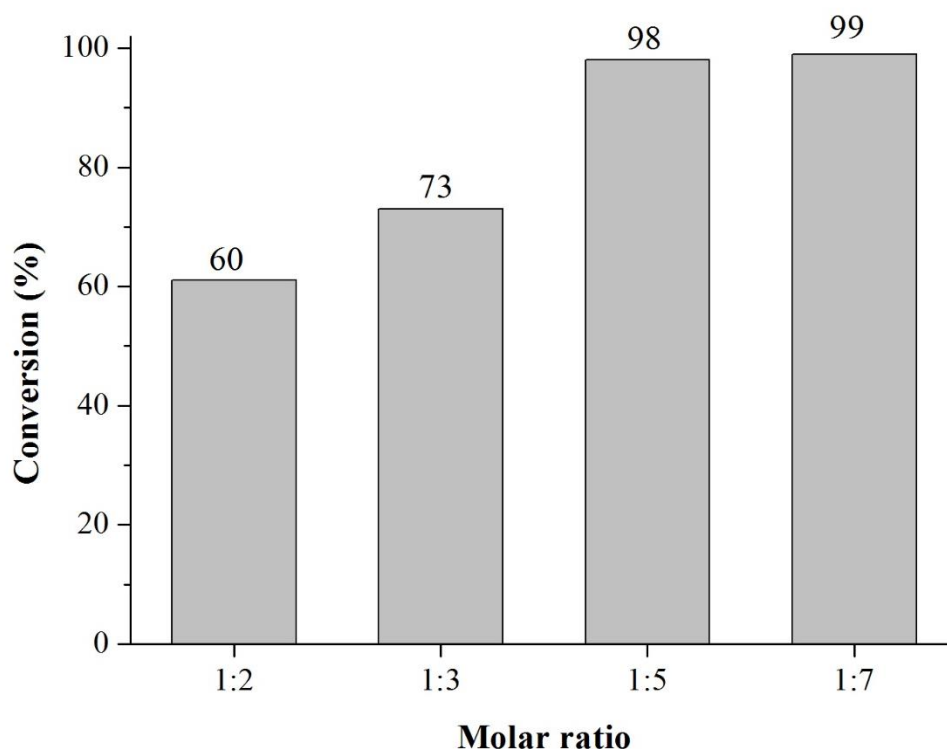


**Figure 8.** Percentage conversions of eugenyl acetate with different molar ratio of eugenol: acetic anhydride. Reaction conditions: reaction temperature 80 °C and reaction time 40 min and 2% catalyst.

### 2.11. Effect of Reaction Time

In order to evaluate the effect of reaction time on eugenol, reactions were allowed for varying durations of 10 to 50 min and the results obtained were shown in Figure 9. As the other reaction conditions were fixed, the reaction time was considered a dominant parameter controlling eugenol acetylation and therefore eugenol conversion. The eugenol conversion rate was 80% after 10 min of reaction but increases as the reaction duration lasts. The highest conversion rate (99.9%) was reached after 40 min. No further increase in eugenol conversion was observed after 50 min. Laroque et al. [31] investigated the acetylation of eugenol over molecular sieves 4Å and reported 90% conversion of eugenol in 2 h, a lower value than that obtained in this work.

The optimum conditions for eugenol acetylation over (3) SO<sub>3</sub>H/AlSiM were: eugenol molar ratio to acetic anhydride 1:5; temperature and reaction time 80 °C and 40 min respectively and amount of catalyst 2%.



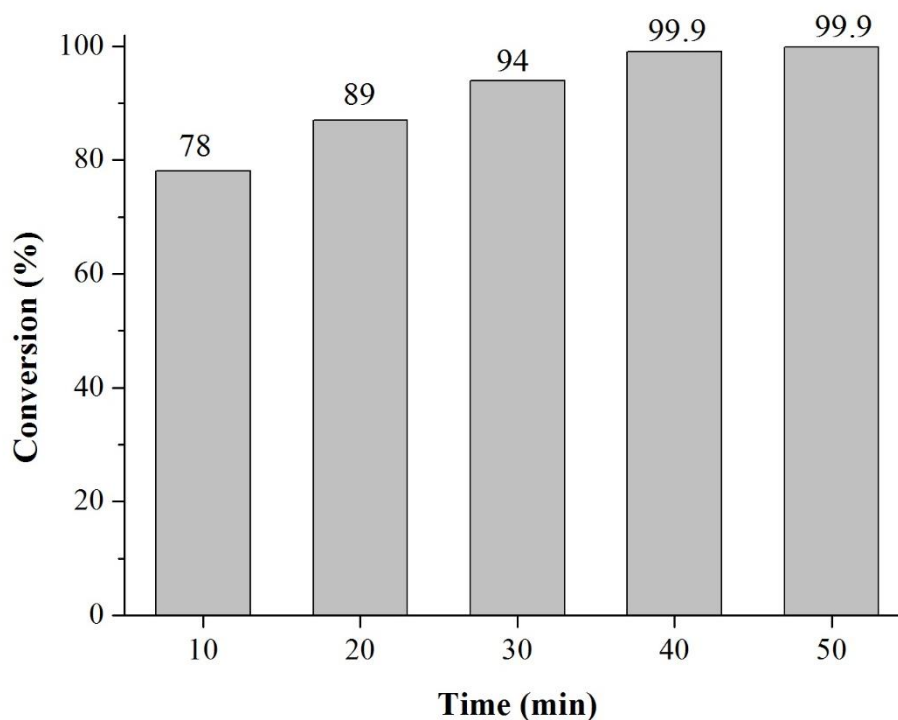


**Figure 9.** Percentage conversions of eugenyl acetate varying the reaction time. Reaction conditions: eugenol: acetic anhydride (1:5), reaction temperature 80 °C and 2% catalyst.

From the high conversion values achieved with the catalyst synthesized here (99.9%) and based on the study of the kinetic parameters of the reaction, it is possible to conclude that the high conversion rates of eugenol, under the reaction conditions reported in this work (Figure 9), were higher than many others reported in literature (Table 5).

Table 5 also presents some results with biocatalysts with maximum conversions of 66% [11] and 93% [5], even if using minimum molar ratio and mild reaction temperature, but reuse inefficiency and high process costs are the disadvantages of the biocatalyst [5,17].

The results revealed that the acid catalyst has a high potential in the acetylation reaction (99.9% conversion). These results are promising not only when compared to solid acid derived from kaolinitic wastes, but also to sulfonated metal oxides. For example, Yadav [10] prepared a zirconia-based catalyst, UDCaT-5, and evaluated it in the esterification of eugenol with benzoic acid, achieving high conversions, at the cost of reaction times and temperatures. Prolonged reaction times have also been observed for commercial catalysts such as molecular sieves 4 Å [31] and *Amberlyst A-21* [32], as well as, full conversion was achieved with Lewatit® GF 101 [17] commercial catalyst. All of the mentioned catalysts used organic solvents, hexane and toluene, during recovery from reuse. Although the conversions obtained in these studies are high, even so, in most cases, the reaction times have always been prolonged when compared to the reaction times used in this work.

It is noteworthy that although hexane and toluene are ideal solvents for the extraction of organic substances, they have all the necessary and appropriate characteristics for catalyst washing. On the other hand, they are highly toxic and harmful to health. In this sense, it was decided to wash or regenerate the catalyst with anhydrous ethanol [24], as it has advantages such as lower cost and is not toxic to animal and human health.

Amazon *flint* kaolin, one of the by-products of the kaolin industry, which presents low cost and high availability, can be perfectly reused in the synthesis of mesoporous molecular sieves, minimizing the use of synthetic silicas, which are often toxic. In addition, kaolin *flint* can be used as a catalytic support or as an alternative heterogeneous catalyst in the acetylation of eugenol with routes to the production of eugenol acetate. Thus, the reuse of this by-product can generate a

reduction in environmental impacts and costs in the synthesis of chemical substances with various applications.

**Table 5.** A comparison of literature results for the conversion of Eugenol over various catalysts.

Catalyst	Solvent	T (°C)	R: M	T (min)	Conv. (%)	Reference
UDCaT-5	Toluene	110	1:5	240	90	[10]
Lipase (RML)	Chloroform	50	1:3	300	66	[11]
Lipozyme TL	Acetic anhydride	70	1:5	120	92.9	[5]
Molecular sieve 4Å	Acetic anhydride	60	1:3	120	90	[31]
Amberlyst A-21	Acetic anhydride	95	1:3	120	95	[32]
Lewatit® GF 101	Acetic anhydride	70	1:1	45	100	[17]
10HPMo/AlSiM	Acetic anhydride	80	1:5	40	99.9	[24]
(3)SO <sub>3</sub> H/AlSiM	Acetic anhydride	80	1:5	40	99.9	Present work

## 2.12. Kinetic Studies

From the kinetic study (Figure 10a) of the different temperatures (50, 60, 70 and 80 °C) and times (10, 20, 30 and 40 min), an estimation was made for the activation energy. The conversion curves of eugenol as a function of time and temperature are observed in Figure 10a, there it is possible note the high performance of (3) SO<sub>3</sub>H/AlSiM for eugenol acetylation when the temperature varies. Santos et al. [67] and Machado et al. [4] reported that increasing the temperature improves both the diffusion and the solubility of the reagents over the reaction time, leading to maximum conversion. As observed also in Figure 10a, high conversions (85%, 90%, 94% and 98%, respectively) were obtained in the first 20 min of reaction.

In this work, we determine the order of the esterification reaction of eugenol with acetic anhydride, using the classical definitions of chemical kinetics and considering eugenol as a limiting reagent [10,31]. To determine the order of reaction by the elementary kinetic theory, we proposed a complete conversion of eugenol. According to data from Figure 10a, it can be concluded that there is a first order dependence between reaction rate and eugenol concentration, because the fit shows a linear relationship between all experimental data when  $-\ln(1-\text{conversion})$  is plotted against reaction time. According to the standard deviations ( $R^2$ ) of 0.9858, 0.9936, 0.9979 and 0.9967 for acetylation carried out at 50, 60, 70 and 80 °C, respectively (Figure 10b). It is observed that the kinetic data analyzed are consistent, as it is a first order reaction in relation to eugenol [10,31]. From the values of  $k$  shown in Figure 10b, plotted  $\ln(k)$  versus  $1/\text{temperature (K)}$  (Figure 10c) and the apparent activation energy ( $E_a$ ) was calculated, which was 17.13 kJ mol<sup>-1</sup> with good linear regression ( $R^2 = 0.9994$ ).

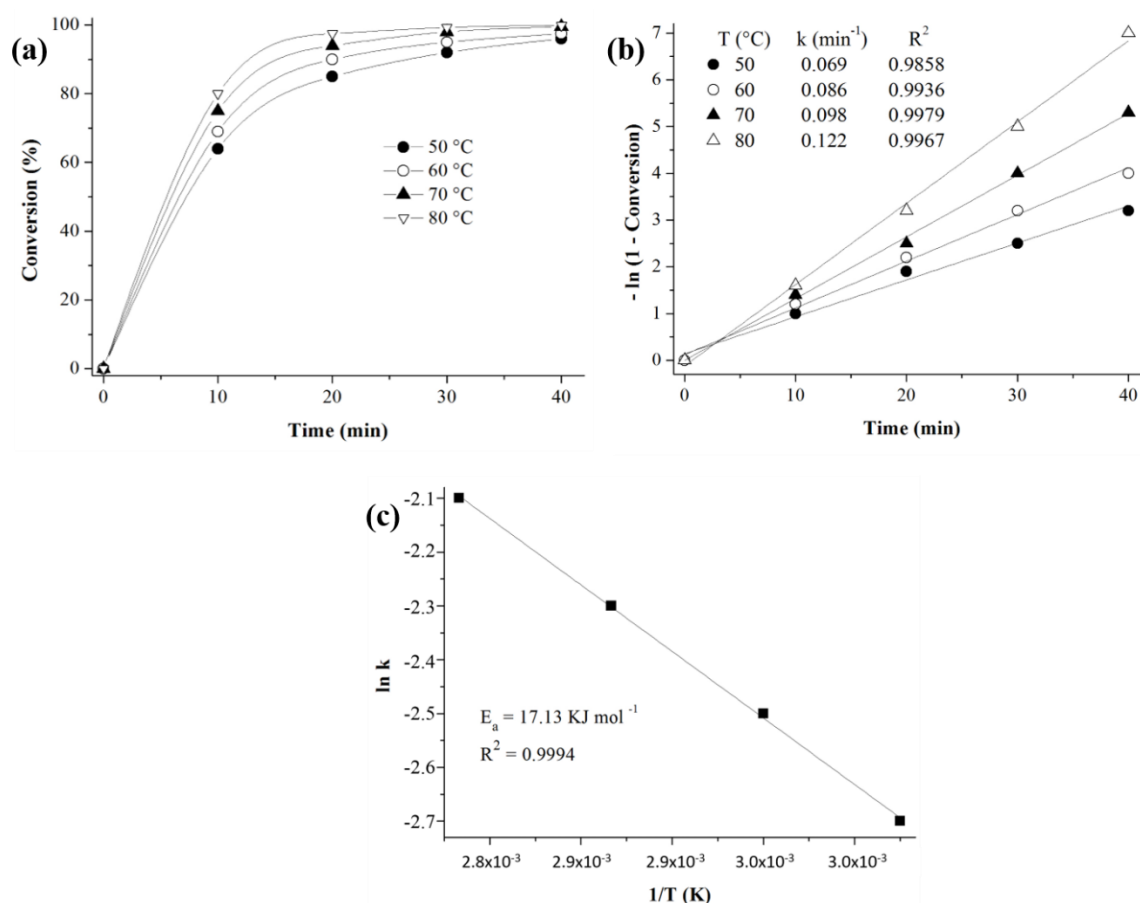


**Figure 10.** (a) Kinetic studies of the conversion of eugenol over the catalysts; (b) graphs of  $-\ln(1 - \text{conversion})$  versus time at different temperatures for calculations of velocity constants and reaction order analysis; (c) Arrhenius graph for calculating the activation energy for eugenol esterification reaction at different temperatures on the catalyst.

The calculation of activation energy can be found in some studies on esterification of eugenol in heterogeneous reaction. For example, Yadav [10] tested the UDCaT-5 catalyst in a heterogeneous esterification reaction and reported a first order reaction in relation to eugenol and an activation energy equivalent to 39.13 kJ mol<sup>-1</sup>. Laroque et al. [31] used two solid catalysts, molecular sieve 4 Å and Amberlite XAD-16, and the kinetic study of acetylation showed a first order reaction with activation energies of 10.03 kJ mol<sup>-1</sup> and 7.23 kJ mol<sup>-1</sup>, respectively. Oliveira et al. [24] applied the 10HPMo/AlSiM catalyst in the same reaction in the acetylation kinetics study found a first order reaction and activation energy equal to 19.96 kJ mol<sup>-1</sup>. Thus, the activation energy obtained in the present work is in the same order of magnitude as those reported in previous works.

The catalyst synthesized here exhibited intermediate activation energy in relation to the different types of solid acid catalysts, related to the esterification of eugenol, which were mentioned in the present manuscript. However, with regards to the reaction conditions, the proposed system operated at a relatively moderate temperature of 80 °C, while those reported had reached 110 °C [10]. In addition, the results of the catalytic tests show that high conversions were achieved by our catalyst within 40 min, and that others from literature achieved comparable conversion only within 4 hours reaction. Obviously, the catalytic performance of (3)SO<sub>3</sub>H/AlSiM is comparatively superior to that of the catalysts we listed for analysis in our study. thus, it is possible to state that (3)SO<sub>3</sub>H/AlSiM is an excellent catalyst for the production of eugenyl acetate, even with an activation energy of 17.13 kJ mol<sup>-1</sup>.

### 2.13. Catalyst Reuse

The use of heterogeneous catalysts is motivated by several factors, including the possibility of reuse in successive cycles, making them essential for reducing production costs and environmentally friendly [10,17,31,32]. Based on this context, the prepared catalyst reuse cycles were evaluated under the same conditions used in the kinetic study. After each cycle of reaction, the catalytic solid was recovered at 6000 rpm for 10 min of centrifugation, washed with ethyl alcohol to remove any organic compounds eventually retained on the support surface, dried in an oven at 150 °C for 2 h subjected to the next catalytic cycle. Ethanol was chosen to perform the washing step based on its good performance, as previously demonstrated for 10HPMo/AlSiM catalyst [24]. The conversion of eugenol after each run (Figure 11) gradually decreases from 99.96% to 92% at the end of the fifth run, revealing an overall reduction close to 8%. These results are slightly better those reported by Oliveira et al. [24] using a solid acid catalyst prepared by anchoring HPMo on an AlSiM mesoporous support to convert eugenol under consecutive runs, revealing a reduction in catalytic activity of approximately 10% after the fifth recycling (90%), compared to the initial value of 99.9%. These eugenol conversion results are excellent, especially considering the low cost associated with this catalyst and the good conversions achieved up to the fifth cycle. These results are even superior to the reaction without the presence of a catalyst (Figure 7), indicating that material can be reused for more reuse cycles. Therefore, it is a clear indication that the catalyst is acting on a heterogeneous route with good catalytic activity using the simple ethanol wash procedure.

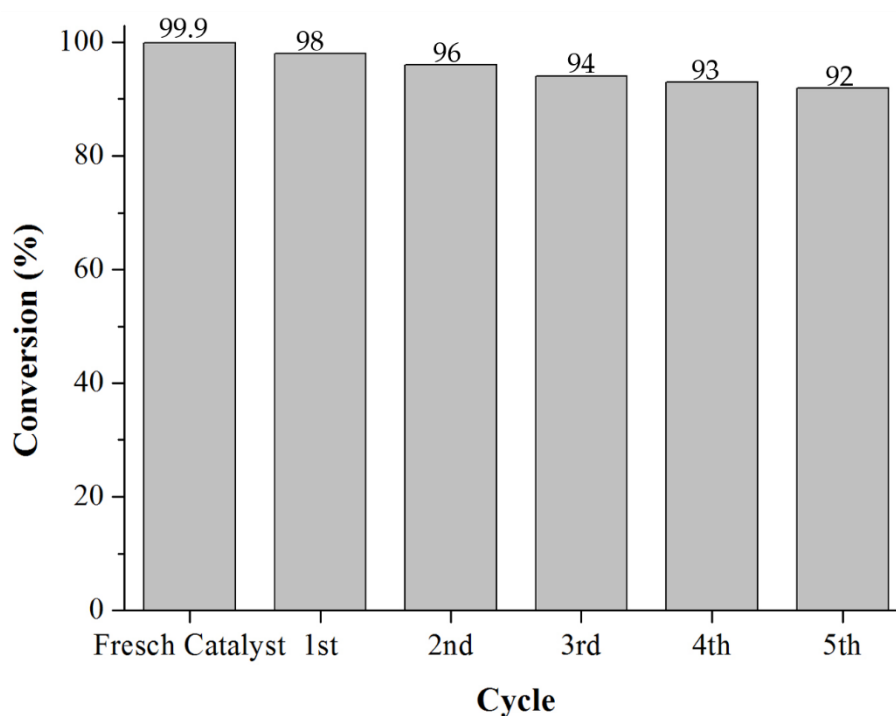


**Figure 11.** Reaction conditions: eugenol: acetic anhydride (1:5), reaction temperature 80 °C, reaction time 40 min and 2% catalyst.

### 2.14. Characterization of Reused Catalyst

After the fifth catalyst reuse cycle, its integrity was assessed by DRX and FTIR techniques. To determine the structural stability of the mesoporous catalyst under eugenol acetylation reaction conditions, the XRD patterns of the samples before ((3) SO<sub>3</sub>H/AlSiM) and after reuse ((3)SO<sub>3</sub>H/AlSiM R) were compared; these results are shown in Figure 12a. After the fifth reuse cycle, a slight decrease in the reflection intensity (100) and a partial disappearance of the reflections (110) and (200) of the reused catalyst can be noted possibly indicating the collapse of the structure to the catalyst used, even so the hexagonal symmetry of the material is still preserved [22,60]. The X-ray diffraction results of

(3)SO<sub>3</sub>H/AlSiM R (Figure 12a) shows little similarity to the diffractogram pattern of the new catalyst. The three reflection peaks of the plane (100) characteristic of the hexagonal structure are observed; as well as two other less intense peaks inherent to the planes (110) and (200) reflections, indicating a material pore system poorly organized [22,60]. This behavior could be associated to molecules adsorbed on the surface as well as inside the channels, consequently indicating a structural disorder of the support (Figure 12a), being one of the reasons for catalyst deactivation during reaction [27]. This result is favorable once, even after successive reuse cycles and despite the recognized fragility of the material, it is observed that its hexagonal structure is preserved [60].

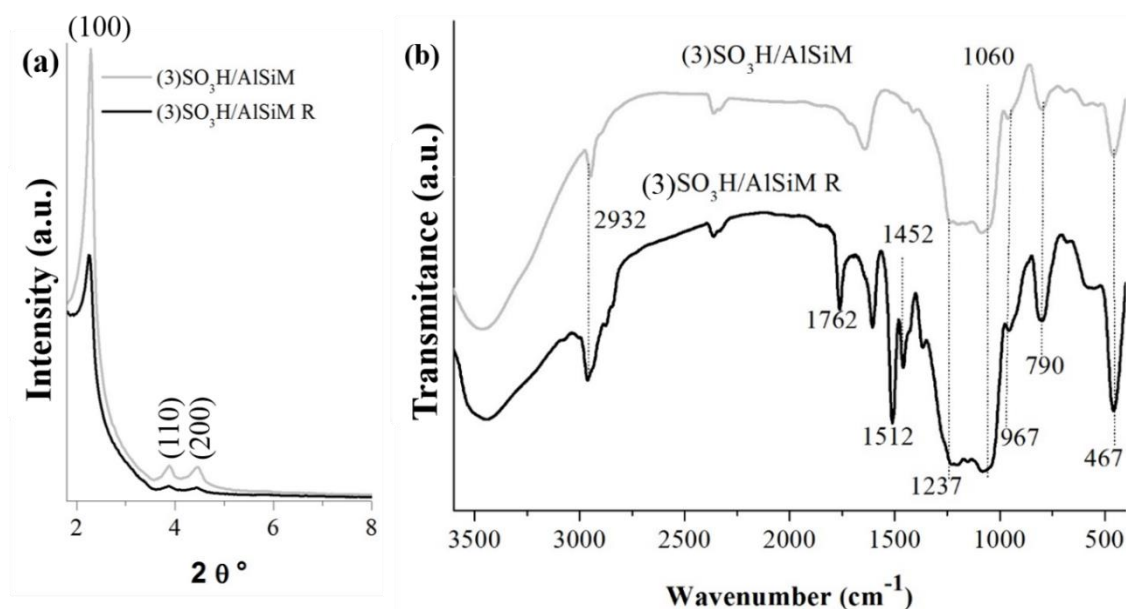


**Figure 12.** (a) Comparison of new catalyst XRD standards, (3)SO<sub>3</sub>H/AlSiM and after reuse, (3)SO<sub>3</sub>H/AlSiM R; (b) Comparison of new catalyst FTIR spectra, (3)SO<sub>3</sub>H/AlSiM, and after reuse (3)SO<sub>3</sub>H/AlSiM R.

The mechanism of adsorption of molecules on the catalyst surface as well as the numerous stages of simultaneous surface reactions was well understood in Scheme 1 and are one of the possible factors (operating conditions) that favor the catalyst deactivation process. The presence of prominent bands of organic groups is clearly noted from the FTIR result. The FTIR Spectrum (Figure 12b) of (3)SO<sub>3</sub>H/AlSiM R showed prominent bands in 2932, 1765, 1513 cm<sup>-1</sup> which were attributed to the stretching vibration of CH, CH<sub>2</sub>/CH<sub>3</sub>, C=O and presence of aromatic ring (C=C) [4,73–76] demonstrating the binding of the esterification product to the surface of the reused catalyst. However, these characterizations showed that there were many differences between new and used catalysts, partially indicating that the catalyst exhibited good structural stability and activity for the eugenol reaction process.

### 3. Materials and Methods

#### 3.1. Materials

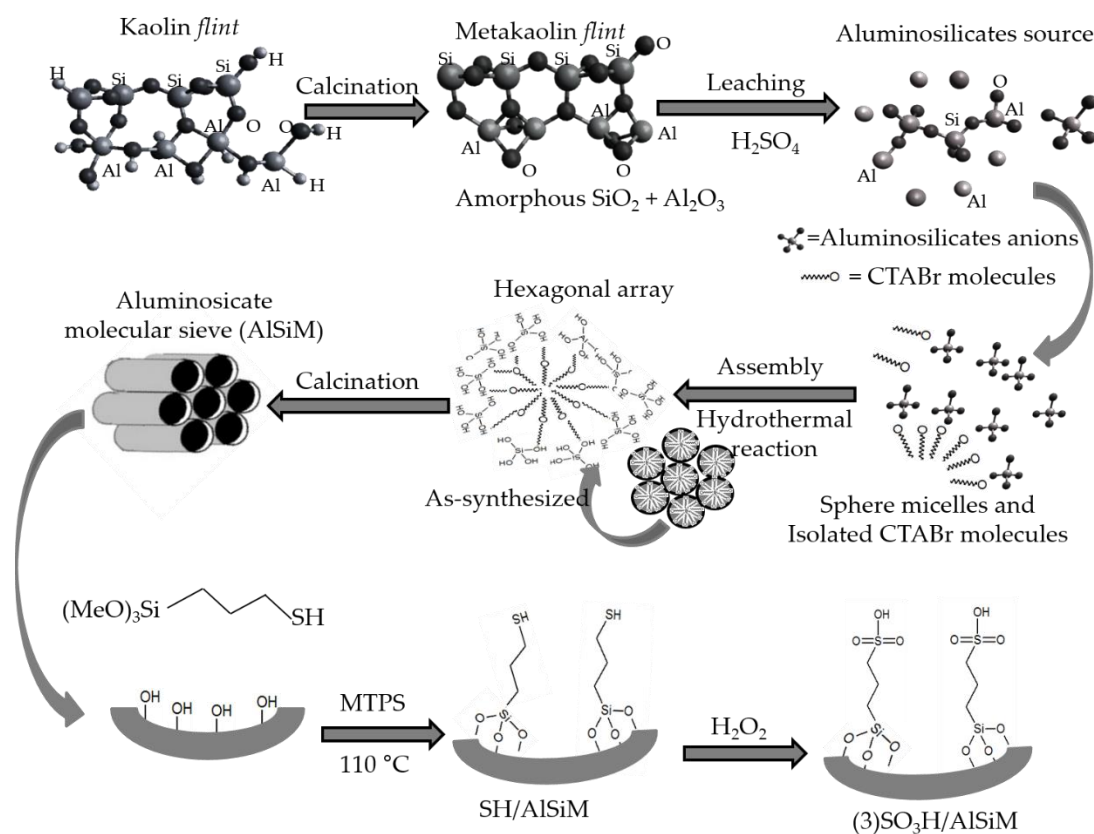
All chemicals used in this experiment were analytical grade and used without further Darmstadt, Germany purification: eugenol (EugOH) (99%, Sigma-Aldrich, Aldrich, San Luis, Missouri, EUA) and acetic anhydride (AA) (nuclear, São Paulo, SP–Brazil), sulfuric acid (H<sub>2</sub>SO<sub>4</sub>) (98%, ISOFAR, Duque de Caxias, Rio de Janeiro, Brazil) 3-mercaptopropyltrimethoxysilane (MPTS) (synthetic grade, Sigma-Aldrich, Aldrich, San Luis, Missouri, EUA), cetyltrimethylammonium bromide (CTABr, Sigma-Aldrich, Aldrich, San Luis, Missouri, EUA), anhydrous ethanol (EtOH) (98%) (synthetic grade, nuclear, São Paulo, SP–Brazil) and sodium hydroxide (NaOH), dichloromethane (CH<sub>2</sub>Cl<sub>2</sub>), diethyl ether (Et<sub>2</sub>O) peroxide hydrogen (H<sub>2</sub>O<sub>2</sub>), toluene (all synthetic

grade, VETEC, Darmstadt, Germany). The *flint* kaolin from the Capim River region (Pará-Brazil), kindly supplied by a partner of Institute of Geosciences (UFPA), was crushed and the sandy fraction separated by sieve retention. The fraction smaller than 62  $\mu\text{m}$  was then collected, diluted in distilled water and centrifuged to separate the silt fraction, obtaining the clay fraction based on the previous work by Nascimento et al. [21,25].

### 3.2. Preparation of Catalysts

#### 3.2.1. Thermal and Acid Treatments of Amazon *Flint* Kaolin

Due to its high content of octahedral aluminum, kaolin is resistant to acid leaching. The calcination of kaolin leads to the formation of the metakaolin phase which makes this material more susceptible to leaching of aluminum and iron cations from the octahedral layer [21,25]. Thus, the clay fraction of the *flint* kaolin (KF) was calcined at 750  $^{\circ}\text{C}$  for 5 h resulting in metakaolin *flint* (MF). The MF sample was leached in a solution of  $\text{H}_2\text{SO}_4$  (2.5  $\text{mol L}^{-1}$ ) in a proportion of 1:10 (MF:  $\text{H}_2\text{SO}_4$ ) for 1 h at 90  $^{\circ}\text{C}$  and then washed with 100 ml of  $\text{H}_2\text{SO}_4$  (0.5  $\text{mol L}^{-1}$ ) and water until pH = 7 is reached and then dried at 120  $^{\circ}\text{C}$  for 12 h. The metakaolin sample obtained was designated as MFL (Scheme 2) [24,28].



**Scheme 2.** Possible formation of AlSiM from natural *flint* kaolin followed by functionalization with MPTS.

#### 3.2.2. Synthesis of Mesoporous Aluminosilicate (AlSiM)

The synthesis of AlSiM was carried out according to the methodology recommended in the literature that obtains mesoporous material at 110  $^{\circ}\text{C}$  in 24 h by hydrothermal treatment [24,28]. The procedure used consists of 3 g of MFL, 0.6172 g of sodium hydroxide, 1.8168 g of hexadecyltrimethylammonium bromide and 134.7 ml of distilled water. The resulting mixture remained stirred for another 24 h and, subsequently, was placed in stainless steel autoclave-coated

teflon vessel. The set was subjected to hydrothermal treatment (110 °C for 24 h). The material obtained was filtered and washed with distilled water and dried in a muffle at 100 °C for 4 h and calcined at 540 °C for 5 h, with a heating ramp of 5 °C min<sup>-1</sup>. The mesoporous material resulting from KF as a source of silica was called AlSiM. A summary of the procedure for preparing AlSiM from natural KF is shown in Scheme 2 [24,36,37,42].

### 3.2.3. Functionalization of AlSiM with MTPS

The AlSiM functionalization process was based on the procedure described by Lima et al. [28] (Scheme 2). Initially, AlSiM was dried at 110 °C for 24 h; then 1 g AlSiM was dispersed in a functionalizing solution with 3 and 5 mmol MPTS in 30 mL of toluene while stirring for 12 h at 110 °C under reflux. After completion of this process, the material was filtered, washed with 50 mL of toluene and dried at 70 °C for 12 h. Excess MPTS, not anchored in AlSiM, was extracted on a Soxhlet extractor with a mixture of CH<sub>2</sub>Cl<sub>2</sub>/Et<sub>2</sub>O (50% v/v) for 12 h, purified solid material (SH/AlSiM) was filtered and dried. Anchored –SH groups were oxidized by immersing 1 g SH/AlSiM in 17 mL H<sub>2</sub>O<sub>2</sub> for 12 h at room temperature. The oxidized material was then washed with H<sub>2</sub>O/EtOH (50% v/v) and extensively with distilled water to neutral pH, dried at 60 °C and stored in a desiccator for further characterization. After all this process, the catalyst was denoted as (x)SO<sub>3</sub>H/AlSiM, where x = mmol of MPTS.

### 3.3. Characterization

The chemical compositions of the samples were obtained with Shimadzu EDX-700 energy dispersive X-ray spectrometer (EDX; EDX-700, SHIMADZU, Kyoto, Japan), with a rhodium X-ray source tube (40 kV, SHIMADZU, Kyoto, Japan). For each analysis, approximately 500 mg (powder) of each sample was deposited in a lower sample holder made of polyethylene film in order to determine the silica content present in the precursor kaolin *flint*.

X-ray diffraction analysis were performed on a Bruker D8 Advance diffractometer (Bruker D8 Advance; Bruker Corp, Billerica, MA, EUA), using powder method, at a 1° < 2θ > 10° interval. Cu Kα (λ = 1.5406 Å, 40 kV e 40 mA) radiation was used. The 2 θ scanning speed was 0.02° min<sup>-1</sup>. The equation  $a_0 = 2d_{100}/\sqrt{3}$  was used to calculate the distance (a<sub>0</sub>) between pore centers of the hexagonal structure [28,34].

N<sub>2</sub> adsorption–desorption isotherms were obtained at liquid nitrogen temperature using a Micromeritics TriStar II model 3020 V1.03 apparatus (Norcross, GA, USA). Before each measurement, the samples were outgassed at 200 °C for 2 h. The specific surface area (SSA) was determined according to the standard Brunauer–Emmett–Teller (BET) method. Pore diameter (D<sub>p</sub>) and pore volume (V<sub>p</sub>) were obtained by the Barret–Joyner–Halenda (BJH) method [55,56,77]. The pore wall thickness (W<sub>t</sub>) was calculated according to equation  $W_t = a_0 - D_p$  [28,34].

The spectroscopy analysis in the infrared region was performed in a Fourier Transform Infrared (FTIR) spectrophotometer from Shimadzu (Kyoto, Japan), model IRPrestige-21 A, using KBr pellets. These pellets were prepared by mixing 0.2 mg of sample with a sufficient amount of KBr to achieve a concentration of 1% by mass. The spectra were obtained in the spectral region from 4000 to 400 cm<sup>-1</sup> with resolution of 4 and 32 scans.

The FTIR technique was used to verify the nature of the acidic sites (Brønsted and Lewis) on the surface of the catalyst having pyridine adsorbed as a probe molecule [24,27,78,79]. The identification of acid sites was performed by preheating about 50 mg of the sample at 120 °C for 90 min, before pyridine treatment with probe molecule. The loosely filled sample was brought in contact with pyridine (about 0.1 cm<sup>3</sup>) directly. Then the sample was kept in a hot air oven at 120 °C for 1 h to remove physisorbed pyridine. After cooling the catalyst sample, the FTIR spectrum was recorded in the spectral range 1700 and 1400 cm<sup>-1</sup> with 256 scans and at a resolution of 4 cm<sup>-1</sup> using KBr background [24,27,78,79].

The thermal decomposition of the AlSiM and (3 or 5) SO<sub>3</sub>H/AlSiM samples was performed on a Shimadzu DTG-60H (Kyoto, Japan) thermogravimetric (TGA/DTG) analyzer. About 10 mg (powder)



of each sample is used for each analysis and placed in a platinum pan and heated from 25 °C to 900 °C, with a heating rate of 10 °C min<sup>-1</sup> and inert gas flow of 50 mL min<sup>-1</sup>.

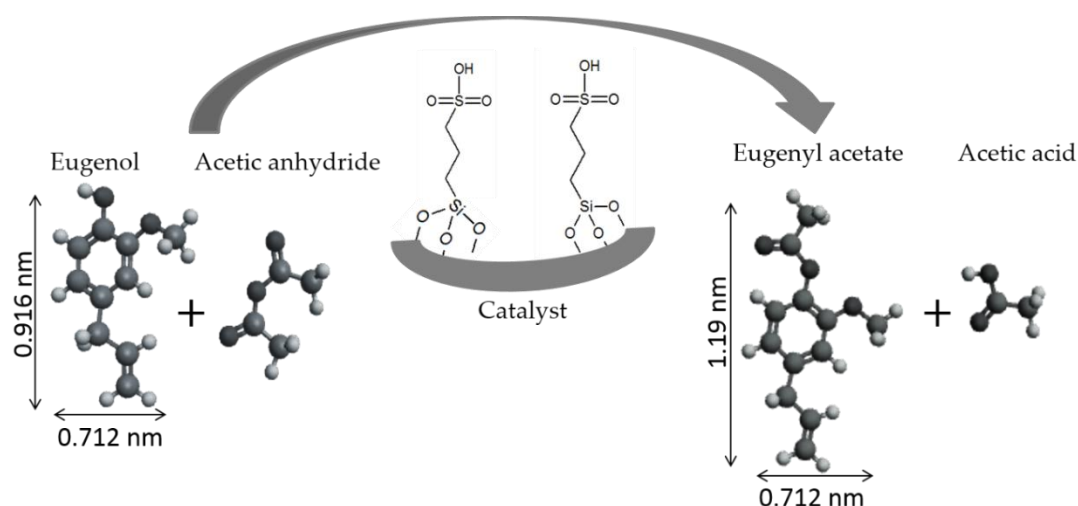
TG Analyses also were used to quantify the number of acid sites. Specifically, the samples prepared for evaluation of the presence of acidic sites in the infrared were submitted to thermal analysis and the TGA/DTG curves of the samples without adsorption and with adsorbed pyridine (Py) were acquired. The difference in mass of the sample before and after being submitted to the adsorption of pyridine was used to calculate the number of acid sites. The value of this difference corresponds to the mass of pyridine adsorbed where each mole of pyridine equals one mole of the acid site present on the surface of the catalyst. From these data the number of mmol of pyridine (nPy) per gram of sample was mathematically determined according to the method proposed by Nascimento et al. [21,25].

Acid-base titrations were used to determine the surface acidity of the catalyst [22,23,27]. In a typical measurement, 0.1 g of solid was suspended in 50 mL of 0.1 M NaOH. The suspension was stirred for 24 h at room temperature and titrated with 0.1 M HCl in the presence of phenolphthalein. The surface acidity of the catalyst was expressed in mmol H<sup>+</sup> g<sup>-1</sup> of catalyst.

### 3.4. Catalytic Tests

#### 3.4.1. Acetylation of Eugenol

The acetylation reaction of eugenol using the catalyst (3) SO<sub>3</sub>H/AlSiM was carried out in a PARR 4871 multi-reactor (Parr Instrument Company, Moline, IL, USA). All experiments were carried out under different reaction temperatures (50, 60, 70 and 80 °C), molar proportions eugenol/acetic anhydride (1:5), quantity of catalyst (2% w/w in eugenol), at 500 rpm for a maximum period of 40 min (Scheme 3). The (3) SO<sub>3</sub>H/AlSiM catalyst was previously dried at 130 °C for 2 h before the reaction. After each experimental run, the catalyst was separated from the reaction medium by centrifugation (6000 rpm for 10 min) and the reaction conversion was determined by gas chromatography (GC/MS).



**Scheme 3.** Design of acetylation of eugenol with acetic anhydride on the catalyst during catalytic tests, molecular size of eugenol ( $l = \sim 0.916$  nm,  $w = \sim 0.712$  nm) and eugenyl acetate ( $l = \sim 1.19$  nm,  $w = \sim 0.712$  nm) by Gaussian software.

The reaction products were quantified by gas chromatography (GC/MS), using Shimadzu equipment (Shimadzu QP2010 plus instrument, Shimadzu Corporation, Kyoto, Japan). A capillary column of fused silica Rtx-5MS (30 m  $\times$  0.25 mm  $\times$  0.25  $\mu\text{m}$ ) was used. Helium (He) was used as carrier gas in a flow of 1.2 mL min<sup>-1</sup>. The injector and detector temperatures were 200 °C and 240 °C, respectively. 1.0  $\mu\text{L}$  of solution of products in 1.5 mL of dichloromethane were injected in the flow division mode (20:1). The programming of the column temperature for the analyzes started at 60 °C,

followed by heating at the rate of 3 °C min<sup>-1</sup> until reaching 240 °C. The mode of operation of the EIMS (electron ionization mass spectrum) was with energy of 70 eV, temperature of the ion source and connection parts, 200 °C. The chemical constituents of the reaction were identified by comparison with the substance library (NIST-11, FFNSC-2) [80] and with data from the literature [73,74]. This analytical procedure was performed at Adolpho Ducke Laboratory—Museu Paraense Emílio Goeldi.

The spectra were scanned within the range  $m/z$  40–300. GC/MS analysis shows the presence of the ester at a retention time of 31.6 min (Figure S2 and Table S1). The mass spectrum of ester product showed a molecular ion peak at  $m/z$  206 that corresponded to molecular formula of eugenyl acetate (C<sub>14</sub>H<sub>14</sub>O<sub>3</sub>). Cleavage of the ester gave the fragment peak at  $m/z$  164 related to the eugenol part [M+H]<sup>+</sup>. Other fragments ions were also observed at  $m/z$  41, 57, 91, 103, 131 and 149 [4,73–76] (Figure S3 and Table S1, see Supplementary Material).

Samples of product (eugenyl acetate) was subjected to FTIR analysis and the spectra were obtained using a Shimadzu model IRPrestige-21A Spectrophotometer. For each sample, the mean of 32 scans in the range 400–4000 cm<sup>-1</sup> and the resolution of 4 cm<sup>-1</sup> was done. The measurements of the samples were normalized by the air background.

The wavelength values obtained in the analyses of eugenyl acetate they are represented in Figure S1, where is observed the presence of the characteristic carbonyl band of the ester linked to the aromatic ring at 1765 cm<sup>-1</sup>, confirming that only the acyl group was added to the eugenol molecule [4,73,76].

#### 4. Conclusions

Based on the characterization techniques employed to study the properties of the new catalyst synthesized by this work, it can be concluded that *flint* kaolin was successfully used as an alternative source of silicon and aluminum for mesoporous catalytic support (AlSiM) synthesis, once that the material obtained has intrinsic properties of mesopore material. The anchoring of sulfonic groups in the AlSiM structure enabled (3) SO<sub>3</sub>H/AlSiM to be active for eugenol acetylation with a maximum conversion of 99.9%. The performance of the catalyst was attributed to its high SSA (998 m<sup>2</sup> g<sup>-1</sup>), V<sub>p</sub> (0.78 cm<sup>3</sup> g<sup>-1</sup>), D<sub>p</sub> (3.25 nm) and strong surface acidity (295 μmol g<sup>-1</sup> of pyridine). material, which favors diffusion regarding the conversion of the substrate and the product. Although successive reuse of the catalyst showed a slight decrease in activity, it nonetheless showed 90% conversion recovery over the fourth cycle, i.e., 92% of the original value (99.9%). The decrease in catalytic activity after each catalyst reuse cycle results from the adsorption of molecules from the reagent or product to their active sites. The integrity of the catalyst before and after the fifth cycle of reuse was confirmed by XRD, which results confirmed that the mesoporous structure was preserved. The good stability, the recyclability and the high catalytic activity in converting eugenol were remarkable characteristics of this new catalyst, which were obtained by a simple method with reduced reaction time and cleaner and lower cost processes. Therefore, that new eco-friendly heterogeneous catalyst was efficient to synthesize a molecule with potential larvicidal activity.

**Supplementary Materials:** The following are available online at [www.mdpi.com/2073-4344/10/5/478/s1](http://www.mdpi.com/2073-4344/10/5/478/s1). Figure S1: Eugenol and Eugenyl acetate FTIR spectra, Figure S2: Mass spectrometry (GC/MS) (a) eugenol, (b) eugenol and eugenol acetate, (c) acetate eugenol, Figure S3: Chromatograms (a) eugenol, (b) eugenol and eugenol acetate (autocatalysis), (c) eugenol and eugenol acetate (catalyzed with (3)SO<sub>3</sub>H/AlSiM), (d) eugenol acetate (catalyzed with (3)SO<sub>3</sub>H/AlSiM). Table S1: Chemical characterization of eugenol and eugenyl acetate by GC/MS.

**Author Contributions:** Conceptualization, L.A.S.d.N.; methodology, E.H.d.A.A., C.E.F.d.C. and G.N.d.R.F.; formal analysis, A.d.N.d.O., L.H.d.O.P. and E.T.L.L.; investigation, A.d.N.d.O., E.T.L.L. and L.H.d.O.P.; resources, E.H.d.A.A., J.R.Z. and C.E.F.d.C.; data curation, R.L. and L.A.S.d.N.; writing—original draft preparation, A.d.N.d.O. and E.T.L.L.; writing—review and editing, J.R.Z. and R.L.; visualization, R.L., G.N.d.R.F. and L.A.S.d.N.; supervision, R.L., C.E.F.d.C., G.N.d.R.F. and L.A.S.d.N.; project administration, R.L. and L.A.S.d.N.; funding acquisition, G.N.d.R.F. and L.A.S.d.N. All authors have read and agreed to the published version of the manuscript.

**Funding:** This research was funded by Banco da Amazônia grant number 2018/212 and CNPQ, grant number 432221/2018-2.

**Acknowledgments:** The authors would like to thank the laboratories that supported this work: Laboratory of Research and Analysis of Fuels (LAPAC/UFGA), Laboratory of Catalysis and Oil Chemistry (LCO/UFGA) and LABNANO-AMAZON/UFGA. CAPES/UNIFAP and PROPESP/UFGA for the financial support.

**Conflicts of Interest:** The authors declare no conflict of interest.

## Reference

- Smith, L.B.; Kasai, S.; Scott, J.G. Pyrethroid resistance in *Aedes aegypti* and *Aedes albopictus*: Important mosquito vectors of human diseases. *Pestic. Biochem. Physiol.* **2016**, *133*, 1–12, doi:10.1016/j.pestbp.2016.03.005.
- Barbosa, J.D.F.; Silva, V.B.; Alves, B.; Gumina, G.; Santos, R.L.C.; Sousa, D.P.; Cavalcanti, S.C.H. Structure—Activity relationships of eugenol derivatives against *Aedes aegypti* (Diptera : Culicidae) larvae. *Pest Manag. Sci.* **2012**, *68*, 1478–1483, doi:10.1002/ps.3331.
- Govindarajan, M.; Rajeswary, M.; Benelli, G. Chemical composition , toxicity and non-target effects of *Pinus kesiya* essential oil: An eco-friendly and novel larvicide against malaria , dengue and lymphatic filariasis mosquito vectors. *Ecotoxicol. Environ. Saf.* **2016**, *129*, 85–90, doi:10.1016/j.ecoenv.2016.03.007.
- Machado, J.R.; Pereira, G.N.; de Oliveira, P.D.S.; Zenevich, M.C.; Lerin, L.; de Oliveira, R.D.R.B.; de Holanda Cavalcanti, S.C.; Ninow, J.L.; de Oliveira, D. Synthesis of eugenyl acetate by immobilized lipase in a packed bed reactor and evaluation of its larvicidal activity. *Process Biochem.* **2017**, *58*, 114–119, doi:10.1016/j.procbio.2017.04.031.
- Silva, M.J.A.; Loss, R.A.; Laroque, D.A.; Lerin, L.A.; Pereira, G.N.; Thon, É.; Oliveira, J.V.; Ninow, J.L.; Hense, H.; Oliveira, D. Lipzyme TL IM as Catalyst for the Synthesis of Eugenyl Acetate in Solvent-Free Acetylation. *Appl. Biochem. Biotechnol.* **2015**, *176*, 782–795, doi:10.1007/s12010-015-1611-5.
- Pandey, S.K.; Tandon, S.; Ahmad, A.; Singh, A.K.; Tripathi, A.K. Structure—Activity relationships of monoterpenes and acetyl derivatives against *Aedes aegypti* (Diptera: Culicidae) larvae. *Pest Manag. Sci.* **2013**, *69*, 1235–1238, doi:10.1002/ps.3488.
- Charan Raja, M.R.; Velappan, A.B.; Chellappan, D.; Debnath, J.; Mahapatra, S.K. Eugenol derived immunomodulatory molecules against visceral leishmaniasis. *Eur. J. Med. Chem.* **2017**, *139*, 503–518, doi:10.1016/j.ejmech.2017.08.030.
- Giovannini, P.P.; Sacchetti, G.; Catani, M.; Massi, A.; Tacchini, M.; De Oliveira, D.; Lerin, L.A. Continuous production of eugenol esters using enzymatic bed microreactors and an evaluation of the products as antifungal agents. *Flavour Fragr. J.* **2019**, *34*, 201–210, doi:10.1002/ffj.3492.
- da Silva, F.F.M.; Monte, F.J.Q.; de Lemos, T.L.G.; do Nascimento, P.G.G.; de Medeiros Costa, A.K.; Paiva, L.M.M. Eugenol derivatives: Synthesis, characterization, and evaluation of antibacterial and antioxidant activities. *Chem. Cent. J.* **2018**, *12*, 34, doi:10.1186/s13065-018-0407-4.
- Yadav, G.D.; Yadav, A.R. Insight into esterification of eugenol to eugenol benzoate using a solid super acidic modified zirconia catalyst UDCaT-5. *Chem. Eng. J.* **2012**, *192*, 146–155, doi:10.1016/j.cej.2012.03.064.
- Manan, F.M.A.; Attan, N.; Zakaria, Z.; Keyon, A.S.A.; Wahab, R.A. Enzymatic esterification of eugenol and benzoic acid by a novel chitosan-chitin nanowhiskers supported Rhizomucor miehei lipase: Process optimization and kinetic assessments. *Enzyme Microb. Technol.* **2018**, *108*, 42–52, doi:10.1016/j.enzmictec.2017.09.004.
- Manan, F.M.A.; Rahman, I.N.A.; Marzuki, N.H.C.; Mahat, N.A.; Huyop, F.; Wahab, R.A. Statistical modelling of eugenol benzoate synthesis using Rhizomucor miehei lipase reinforced nanobioconjugates. *Process Biochem.* **2016**, *51*, 249–262, doi:10.1016/j.procbio.2015.12.002.
- Cansian, R.L.; Vanin, A.B.; Orlando, T.; Piazza, S.P.; Puto, B.M.S.; Cardoso, R.I.; Gonçalves, I.L.; Honaiser, T.C.; Paroul, N.; Oliveira, D. Toxicity of clove essential oil and its ester eugenyl acetate against *Artemia salina*. *Braz. J. Biol.* **2017**, *77*, 155–161, doi:10.1590/1519-6984.12215.
- Teixeira, R.R.; Gazolla, P.A.R.; da Silva, A.M.; Borsodi, M.P.G.; Bergmann, B.R.; Ferreira, R.S.; Vaz, B.G.; Vasconcelos, G.A.; Lima, W.P. Synthesis and leishmanicidal activity of eugenol derivatives bearing. *Eur. J. Med. Chem.* **2018**, *146*, 274–286, doi:10.1016/j.ejmech.2018.01.046.
- Slamenová, D.; Horváthová, E.; Wsólóvá, L.; Sramková, M.; Navarová, J. Investigation of anti-oxidative , cytotoxic , DNA-damaging and DNA-protective effects of plant volatiles eugenol and borneol in human-derived HepG2, Caco-2 and VH10 cell lines. *Mutat. Res.* **2009**, *677*, 46–52, doi:10.1016/j.mrgentox.2009.05.016.

16. Sadeghian, H.; Seyedi, S.M.; Saberi, M.R.; Arghiani, Z.; Riazi, M. Design and synthesis of eugenol derivatives, as potent 15-lipoxygenase inhibitors. *Bioorganic Med. Chem.* **2008**, *16*, 890–901, doi:10.1016/j.bmc.2007.10.016.
17. Tischer, J.S.; Possan, H.; Luiz, J.; Malagutti, N.B.; Matello, R.; Valério, A.; Dalmagro, J.; De Oliveira, D.; Oliveira, J.V. Synthesis of eugenyl acetate through heterogeneous catalysis. *J. Essent. Oil Res.* **2019**, *31*, 312–318, doi:10.1080/10412905.2019.1566098.
18. Chiaradia, V.; Paroul, N.; Cansian, R.L.; Júnior, C.V.; Detofol, M.R.; Lerin, L.A.; Oliveira, J.V.; Oliveira, D. Synthesis of eugenol esters by lipase-catalyzed reaction in solvent-free system. *Appl. Biochem. Biotechnol.* **2012**, *168*, 742–751, doi:10.1007/s12010-012-9814-5.
19. Narkhede, N.; Patel, A.; Singh, S. Mono lacunary phosphomolybdate supported on MCM-41: Synthesis, characterization and solvent free aerobic oxidation of alkenes and alcohols. *Dalton Trans.* **2014**, *43*, 2512–2520, doi:10.1039/c3dt52395k.
20. Nascimento, L.A.S.; Angélica, R.S.; Costa, C.E.F.; Zamian, J.R.; Rocha Filho, G.N. Conversion of waste produced by the deodorization of palm oil as feedstock for the production of biodiesel using a catalyst prepared from waste material. *Bioresour. Technol.* **2011**, *102*, 8314–8317, doi:10.1016/j.biortech.2011.06.004.
21. Nascimento, L.A.S.; Angélica, R.S.; Costa, C.E.F.; Zamian, J.R.; Rocha Filho, G.N. Comparative study between catalysts for esterification prepared from kaolins. *Appl. Clay Sci.* **2011**, *51*, 267–273, doi:10.1016/j.clay.2010.11.030.
22. Pires, L.H.O.; Oliveira, A.N.; Monteiro Junior, O.V.; Angélica, R.S.; Costa, C.E.F.; Zamian, J.R.; Nascimento, L.A.S.; Rocha Filho, G.N. Esterification of a waste produced from the palm oil industry over 12-tungstophosphoric acid supported on kaolin waste and mesoporous materials. *Appl. Catal. B Environ.* **2014**, *160–161*, 122–128, doi:10.1016/j.apcatb.2014.04.039.
23. Oliveira, A.N.; da Costa, L.R.S.; Pires, L.H.O.; Nascimento, L.A.S.; Angélica, R.S.; Da Costa, C.E.F.; Zamian, J.R.; Da Rocha Filho, G.N. Microwave-assisted preparation of a new esterification catalyst from wasted flint kaolin. *Fuel* **2013**, *103*, 626–631, doi:10.1016/j.fuel.2012.07.017.
24. Oliveira, A.N.; Lima, E.T.L.; Oliveira, D.T.; Andrade, E.H.A.; Angélica, R.S.; Costa, C.E.F.; Rocha Filho, G.N.; Costa, F.F.; Luque, R.; Nascimento, L.A.S. Acetylation of Eugenol over 12-Molybdophosphoric Acid Anchored in Mesoporous Silicate Support Synthesized from Flint Kaolin. *Materials (Basel)* **2019**, *12*, 2995, doi:10.3390/ma12182995.
25. Nascimento, L.A.S.; Tito, L.M.Z.; Angélica, R.S.; Costa, C.E.F.; Zamian, J.R.; Rocha Filho, G.N. Esterification of oleic acid over solid acid catalysts prepared from Amazon flint kaolin. *Appl. Catal. B Environ.* **2011**, *101*, 495–503, doi:10.1016/j.apcatb.2010.10.021.
26. Carmo, A.C.; de Souza, L.K.C.; da Costa, C.E.F.; Longo, E.; Zamian, J.R.; da Rocha Filho, G.N. Production of biodiesel by esterification of palmitic acid over mesoporous aluminosilicate Al-MCM-41. *Fuel* **2009**, *88*, 461–468, doi:10.1016/j.fuel.2008.10.007.
27. Oliveira, A.N.; Lima, M.A.B.; Pires, L.H.O.; Silva, M.R.; Luz, P.T.S.; Angélica, R.S.; Rocha Filho, G.N.; Costa, C.E.F.; Luque, R.; Nascimento, L.A.S. Bentonites Modified with Phosphomolybdic Heteropolyacid (HPMo) for Biowaste to Biofuel Production. *Materials (Basel)* **2019**, *12*, 1431, doi:10.3390/ma12091431.
28. Lima, E.T.L.; Queiroz, L.S.; de Pires, L.H.O.; Angélica, R.S.; Costa, C.E.F.; Zamian, J.R.; Rocha Filho, G.N.; Luque, R.; Nascimento, L.A.S. Valorization of Mining Waste in the Synthesis of Organofunctionalized Aluminosilicates for the Esterification of Waste from Palm Oil Deodorization. *ACS Sustain. Chem. Eng.* **2019**, *7*, 7543–7551, doi:10.1021/acssuschemeng.8b05484.
29. Queiroz, R.M.; Pires, L.H.O.; de Souza, R.C.P.; Zamian, J.R.; de Souza, A.G.; da Rocha Filho, G.N.; da Costa, C.E.F. Thermal characterization of hydrotalcite used in the transesterification of soybean oil. *J. Therm. Anal. Calorim.* **2009**, *97*, 163–166, doi:10.1007/s10973-009-0246-6.
30. Coral, N.; Rodrigues, E.; Rumjanek, V.; Emmerson, C. Soybean biodiesel methyl esters, free glycerin and acid number quantification by <sup>1</sup>H nuclear magnetic resonance spectroscopy. *Magn. Reson. Chem.* **2013**, *51*, 69–71, doi:10.1002/mrc.3913.
31. Laroque, D.A.; Loss, R.A.; Silva, M.J.A.; Pereira, G.N.; Valerio, A.; Hense, H.; de Oliveira, D.; Oliveira, V. Synthesis of Eugenyl Acetate in Solvent-Free Acetylation: Process Optimization and Kinetic Evaluation. *J. Chem. Eng. Process Technol.* **2015**, *6*, 4–11, doi:10.4172/2157-7048.1000247.
32. Lerin, L.A.; Catani, M.; Oliveira, D.; Massi, A.; Bortolini, O.; Cavazzini, A.; Giovannini, P.P. Continuous ion-exchange resin catalysed esterification of eugenol for the optimized production of eugenyl acetate using a packed bed microreactor. *RSC Adv.* **2015**, *5*, 76898–76903, doi:10.1039/C5RA08457A.

33. De Souza, L.K.C.; Pardaul, J.J.R.; Zamian, J.R.; Geraldo, N.; Filho, R.; Barrado, C.M.; Angélica, R.S.; Carlos, E.F. Rapid synthesis and characterization of CeMCM-41. *Powder Technol.* **2012**, *229*, 1–6, doi:10.1016/j.powtec.2012.04.043.
34. Pires, L.H.O.; Queiroz, R.M.; Souza, R.P.; Carlos, E.F.; Zamian, J.R.; Weber, I.T.; Geraldo, N.; Filho, R. Synthesis and characterization of spherical Tb-MCM-41. *J. Alloys Compd.* **2010**, *490*, 667–671, doi:10.1016/j.jallcom.2009.10.134.
35. De Souza, L.K.C.; Pardaul, J.J.R.; Zamian, J.R.; da Rocha Filho, G.N.; Costa, C.E.F. Influence of the incorporated metal on template removal from MCM-41 type mesoporous materials. *J. Therm. Anal. Calorim.* **2011**, *106*, 355–361, doi:10.1007/s10973-011-1295-1.
36. Zhou, C.; Sun, T.; Gao, Q.; Alshameri, A.; Zhu, P.; Wang, H.; Qiu, X.; Ma, Y.; Yan, C. Synthesis and characterization of ordered mesoporous aluminosilicate molecular sieve from natural halloysite. *J. Taiwan Inst. Chem. Eng.* **2014**, *45*, 1073–1079, doi:10.1016/j.jtice.2013.09.030.
37. Xie, Y.; Zhang, Y.; Ouyang, J.; Yang, H. Mesoporous material Al-MCM-41 from natural halloysite. *Phys. Chem. Miner.* **2014**, *41*, 497–503, doi:10.1007/s00269-014-0660-6.
38. Santos, E.C.; Costa, L.S.; Oliveira, E.S.; Bessa, R.A.; Freitas, A.D.L.; Oliveira, C.P.; Nascimento, R.F.; Loiola, A.R. Al-MCM-41 synthesized from kaolin via hydrothermal route: Structural characterization and use as an efficient adsorbent of methylene blue. *J. Braz. Chem. Soc.* **2018**, *29*, 2378–2386, doi:10.21577/0103-5053.20180115.
39. Wang, G.; Wang, Y.; Liu, Y.; Liu, Z.; Guo, Y.; Liu, G.; Yang, Z.; Xu, M.; Wang, L. Synthesis of highly regular mesoporous Al-MCM-41 from metakaolin. *Appl. Clay Sci.* **2009**, *44*, 185–188, doi:10.1016/j.clay.2008.12.002.
40. Madhusoodana, C.D.; Kameshima, Y.; Nakajima, A.; Okada, K.; Kogure, T.; MacKenzie, K.J.D. Synthesis of high surface area Al-containing mesoporous silica from calcined and acid leached kaolinites as the precursors. *J. Colloid Interface Sci.* **2006**, *297*, 724–731, doi:10.1016/j.jcis.2005.10.051.
41. Kang, F.; Wang, Q.; Xiang, S. Synthesis of mesoporous Al-MCM-41 materials using metakaolin as aluminum source. *Mater. Lett.* **2005**, *59*, 1426–1429, doi:10.1016/j.matlet.2004.11.057.
42. Du, C.; Yang, H. Investigation of the physicochemical aspects from natural kaolin to Al-MCM-41 mesoporous materials. *J. Colloid Interface Sci.* **2012**, *369*, 216–222, doi:10.1016/j.jcis.2011.12.041.
43. Rocha Junior, C.A.F.; Angélica, R.S.; Neves, R.F. Synthesis of faujasite-type zeolite: Comparison between processed and flint kaolin. *Cerâmica* **2015**, *61*, 259–268, doi:10.1590/0366-69132015613581900.
44. Carneiro, B.S.; Angélica, R.S.; Scheller, T.; de Castro, E.A.S.; de Neves, R.F. Mineralogical and geochemical characterization of the hard kaolin from the Capim region, Pará, northern Brazil. *Cerâmica* **2003**, *49*, 237–244, doi:10.1590/S0366-69132003000400008.
45. Sun, C.; Zhang, F.; Wang, X.; Cheng, F. Facile Preparation of Ammonium Molybdophosphate/Al-MCM-41 Composite Material from Natural Clay and Its Use in Cesium Ion Adsorption. *Eur. J. Inorg. Chem.* **2015**, *2015*, 2125–2131, doi:10.1002/ejic.201500114.
46. Sun, C.; Zhang, F.; Li, S.; Cheng, F. Synthesis of SBA-15 encapsulated ammonium molybdophosphate using Qaidam natural clay and its use in cesium ion adsorption. *RSC Adv.* **2015**, *5*, 35453–35460, doi:10.1039/C5RA02398J.
47. Díaz, U.; Brunel, D.; Corma, A. Catalysis using multifunctional organosiliceous hybrid materials. *Chem. Soc. Rev.* **2013**, *42*, 4083–4097, doi:10.1039/c2cs35385g.
48. Ng, E.; Norbayu, S.; Subari, M.; Marie, O.; Mukti, R.R.; Juan, J. Sulfonic acid functionalized MCM-41 as solid acid catalyst for tert -butylation of hydroquinone enhanced by microwave heating. *Appl. Catal. A Gen.* **2013**, *450*, 34–41, doi:10.1016/j.apcata.2012.09.055.
49. Wang, Y.; Fang, Z.; Zhang, F. Esterification of oleic acid to biodiesel catalyzed by a highly acidic carbonaceous catalyst. *Catal. Today* **2019**, *319*, 172–181, doi:10.1016/j.cattod.2018.06.041.
50. Boveri, M.; Aguilar-Pliego, J.; Pérez-Pariente, J.; Sastre, E. Optimization of the preparation method of HSO<sub>3</sub>-functionalized MCM-41 solid catalysts. *Catal. Today* **2005**, *107–108*, 868–873, doi:10.1016/j.cattod.2005.07.033.
51. Guo, K.; Han, F.; Arslan, Z.; McComb, J.; Mao, X.; Zhang, R.; Sudarson, S.; Yu, H. Adsorption of Cs from Water on Surface-Modified MCM-41 Mesosilicate. *Water Air Soil Pollut.* **2015**, *226*, 2–9, doi:10.1007/s11270-015-2565-5.
52. Fontes, M.S.B.; Melo, D.M.A.; Costa, C.C.; Braga, R.M.; Melo, M.A.F.; Alves, J.A.B.L.R.; Silva, M.L.P. Effect of different silica sources on textural parameters of molecular sieve MCM-41. *Cerâmica* **2016**, *62*, 85–90.

53. Kumar, P.; Mal, N.; Oumi, Y.; Yamana, K.; Sano, T. Mesoporous materials prepared using coal fly ash as the silicon and aluminium source. *J. Mater. Chem.* **2001**, *11*, 3285–3290, doi:10.1039/b104810b.
54. Yang, H.; Deng, Y.; Du, C.; Jin, S. Novel synthesis of ordered mesoporous materials Al-MCM-41 from bentonite. *Appl. Clay Sci.* **2010**, *47*, 351–355, doi:10.1016/j.clay.2009.11.050.
55. Sing, K. The use of nitrogen adsorption for the characterisation of porous materials. *Colloids Surf. A Physicochem. Eng. Asp.* **2001**, *187–188*, 3–9, doi:10.1016/S0927-7757(01)00612-4.
56. Sing, K.S.W.; Everett, D.H.; Haul, R.A.W.; Moscou, L.; Pierotti, A.R.; Rouquérol, J.; Siemieniewska, T. Reporting Physisorption Data for Gas/Solid Systems including catalysis reporting physisorption data for gas/solid systems with Special Reference to the Determination of Surface Area and Porosity. *Pure Appl. Chem.* **1985**, *57*, 603–619, doi:10.1515/iupac.57.0007.
57. Patel, A.; Brahmkhatri, V. Kinetic study of oleic acid esterification over 12-tungstophosphoric acid catalyst anchored to different mesoporous silica supports. *Fuel Process. Technol.* **2013**, *113*, 141–149, doi:10.1016/j.fuproc.2013.03.022.
58. Brahmkhatri, V.; Patel, A. 12-Tungstophosphoric acid anchored to SBA-15: An efficient, environmentally benign reusable catalysts for biodiesel production by esterification of free fatty acids. *Appl. Catal. A Gen.* **2011**, *403*, 161–172, doi:10.1016/j.apcata.2011.06.027.
59. Ahmed, A.I.; Samra, S.E.; El-Hakam, S.A.; Khder, A.S.; El-Shenawy, H.Z.; El-Yazeed, W.S.A. Characterization of 12-molybdophosphoric acid supported on mesoporous silica MCM-41 and its catalytic performance in the synthesis of hydroquinone diacetate. *Appl. Surf. Sci.* **2013**, *282*, 217–225, doi:10.1016/j.apsusc.2013.05.105.
60. Méndez, F.J.; Llanos, A.; Echeverría, M.; Jáuregui, R.; Villasana, Y.; Díaz, Y.; Liendo-Polanco, G.; Ramos-García, M.A.; Zoltan, T.; Brito, J.L. Mesoporous catalysts based on Keggin-type heteropolyacids supported on MCM-41 and their application in thiophene hydrodesulfurization. *Fuel* **2013**, *110*, 249–258, doi:10.1016/j.fuel.2012.11.021.
61. Costa, B.O.D.; Legnoverde, M.S.; Lago, C.; Decolatti, H.P.; Querini, C.A. Microporous and Mesoporous Materials Sulfonic functionalized SBA-15 catalysts in the gas phase glycerol dehydration. Thermal stability and catalyst deactivation. *Microporous Mesoporous Mater.* **2016**, *230*, 66–75, doi:10.1016/j.micromeso.2016.04.035.
62. Adam, F.; Kueh, C.W. Phenyl-amino sulfonic solid acid-MCM-41 complex: A highly active and selective catalyst for the synthesis of mono-alkylated products in the solvent free tert-butylation of phenol. *J. Taiwan Inst. Chem. Eng.* **2014**, *45*, 713–723, doi:10.1016/j.jtice.2013.07.008.
63. Zhang, P.; Wu, H.; Fan, M.; Sun, W.; Jiang, P.; Dong, Y. Direct and postsynthesis of tin-incorporated SBA-15 functionalized with sulfonic acid for efficient biodiesel production. *Fuel* **2019**, *235*, 426–432, doi:10.1016/j.fuel.2018.08.029.
64. Lima, E.T.L. Síntese de Al-MCM-41 a partir do rejeito do caulim e impregnação com grupo sulfônico para fins catalíticos. 2016, 63f. In *Dissertação (Mestrado em Química)–Programa de Pós-Graduação em Química*; University Federal do Pará: Belém, Brazil, 2016.
65. Campelo, J.M.; Lafont, F.; Marinas, J.M.; Ojeda, M. Studies of catalyst deactivation in methanol conversion with high, medium and small pore silicoaluminophosphates. *Appl. Catal. A Gen.* **2000**, *192*, 85–96, doi:10.1016/S0926-860X(99)00329-4.
66. Gang, L.; Xinzong, L.; Eli, W. Solvent-free esterification catalyzed by surfactant-combined catalysts at room temperature. *New J. Chem.* **2007**, *31*, 348, doi:10.1039/b615448d.
67. Santos, P.; Zabot, G.L.; Meireles, M.A.A.; Mazutti, M.A.; Martínez, J. Synthesis of eugenyl acetate by enzymatic reactions in supercritical carbon dioxide. *Biochem. Eng. J.* **2016**, *114*, 1–9, doi:10.1016/j.bej.2016.06.018.
68. Narkhede, N.; Singh, S.; Patel, A. Recent progress on supported polyoxometalates for biodiesel synthesis via esterification and transesterification. *Green Chem.* **2015**, *17*, 89–107, doi:10.1039/c4gc01743a.
69. Wang, A.; Wang, J.; Lu, C.; Xu, M.; Lv, J.; Wu, X. Esterification for biofuel synthesis over an eco-friendly and efficient kaolinite-supported  $\text{SO}_{42-}/\text{ZnAl}_2\text{O}_4$  macroporous solid acid catalyst. *Fuel* **2018**, *234*, 430–440, doi:10.1016/j.fuel.2018.07.041.
70. Hoo, P.; Abdullah, A.Z. Kinetics Modeling and Mechanism Study for Selective Esterification of Glycerol with Lauric Acid Using 12-Tungstophosphoric Acid Post-Impregnated SBA-15. *Ind. Eng. Chem. Res.* **2015**, *54*, 7852–7858, doi:10.1021/acs.iecr.5b02304.

71. Baskaran, Y.; Periyasamy, V.; Carani, A. Investigation of antioxidant , anti-inflammatory and DNA-protective properties of eugenol in thioacetamide-induced liver injury in rats. *Toxicology* **2010**, *268*, 204–212, doi:10.1016/j.tox.2009.12.018.
72. Devi, K.P.; Nisha, S.A.; Sakthivel, R.; Pandian, S.K. Eugenol (an essential oil of clove) acts as an antibacterial agent against Salmonella typhi by disrupting the cellular membrane. *J. Ethnopharmacol.* **2010**, *130*, 107–115, doi:10.1016/j.jep.2010.04.025.
73. Santin, J.R.; Lemos, M.; Klein-Júnior, L.C.; Machado, I.D.; Costa, P.; De Oliveira, A.P.; Tilia, C.; De Souza, J.P.; De Sousa, J.P.B.; Bastos, J.K.; et al. Gastroprotective activity of essential oil of the *Syzygium aromaticum* and its major component eugenol in different animal models. *Naunyn-Schmiedeberg's Arch. Pharmacol.* **2011**, *383*, 149–158, doi:10.1007/s00210-010-0582-x.
74. Rodrigues, T.; Fernandes, A., Jr.; Sousa, J.; Bastos, J.; Sforcin, J. In vitro and in vivo effects of clove on pro-inflammatory cytokines production by macrophages. *Nat. Prod. Res.* **2009**, *23*, 319–326, doi:10.1080/14786410802242679.
75. Chaibakhsh, N.; Basri, M.; Anuar, S.H.M.; Rahman, M.B.A.; Rezayee, M. Optimization of enzymatic synthesis of eugenol ester using statistical approaches. *Biocatal. Agric. Biotechnol.* **2012**, *1*, 226–231, doi:10.1016/j.bcab.2012.03.005.
76. Affonso, R.S.; Lessa, B.; Slana, G.B.C.A.; Barboza, L.L.; de Almeida, F.V.; de Souza, F.R.; França, T.C.C. Quantification and Characterization of the Main Components of the Ethanolic Extract of Indian Cloves, *Syzygium aromaticum* [I] Mer. et Perry. *Rev. Virtual Quim.* **2014**, *6*, 1316–1331, doi:10.5935/1984-6835.20140086.
77. Brunauer, S.; Emmett, P.H.; Teller, E. Adsorption of Gases in Multimolecular Layers. *J. Am. Chem. Soc.* **1938**, *60*, 309–319, doi:10.1021/ja01269a023.
78. Reddy, C.R.; Nagendrappa, G.; Prakash, B.S.J. Surface acidity study of Mn<sup>+</sup>-montmorillonite clay catalysts by FT-IR spectroscopy: Correlation with esterification activity. *Catal. Commun.* **2007**, *8*, 241–246, doi:10.1016/j.catcom.2006.06.023.
79. Reddy, C.R.; Bhat, Y.S.; Nagendrappa, G.; Prakash, B.S.J. Brønsted and Lewis acidity of modified montmorillonite clay catalysts determined by FT-IR spectroscopy. *Catal. Today* **2009**, *141*, 157–160, doi:10.1016/j.cattod.2008.04.004.
80. NIST NIST (2011) National Institute of Standard and Technology (2011) NIST Standard Reference Database Number 69. Available online: <http://webbook.nist.gov/> (accessed on 25 November 2018. ).



© 2020 by the authors. Licensee MDPI, Basel, Switzerland. This article is an open access article distributed under the terms and conditions of the Creative Commons Attribution (CC BY) license (<http://creativecommons.org/licenses/by/4.0/>).